Fall 2017

Thermally Assisted Pulsed Electric Field Ablation for Cancer Therapy

James Michael Hornef
Old Dominion University, jhornef@yahoo.com

THERMALLY ASSISTED PULSED ELECTRIC FIELD ABLATION FOR CANCER THERAPY

by

James Michael Hornef
B.S. August 2016, Old Dominion University

A Thesis Submitted to the Faculty of
Old Dominion University in Partial Fulfillment of the
Requirements for the Degree of

MASTER OF SCIENCE

BIOMEDICAL ENGINEERING

OLD DOMINION UNIVERSITY
December 2017

Approved by:

Chunqi Jiang (Director)

Stephen Beebe (Member)

Siqi Guo (Member)

Michel Audette (Member)

ABSTRACT

THERMALLY ASSISTED PULSED ELECTRIC FIELD ABLATION FOR CANCER THERAPY

James Michael Hornef
Old Dominion University, 2017
Director: Dr. Chunqi Jiang

Pulsed Electric Fields (PEF) have promised improved treatment results in a variety of cancer types including melanoma, pancreatic and lung squamous cancer. Recent studies show that PEF-based cancer therapy may be improved further with the assistance of moderate heating of the target. Experiments were performed to design, calibrate and implement a feedback-looped infrared laser irradiation system that could maintain specified temperatures during the treatment. The exact treatment area, penetration depth and thermal distribution of a 980-nm laser fiber were quantified using several methods, including the knife-edge technique and a tissue optical property study. *In vivo* and *in vitro* experiments using this protocol show that there is a synergistic effect between PEF and the moderately elevated heating of a target, which resulted in an increased overall treatment area up to a factor of 5.6 *in vitro* as well as an increased the overall survival of the mice by 54% in the treatment of pancreatic cancer in mice.

This thesis is dedicated to never ending thirst for knowledge and creation of new ideas.

ACKNOWLEDGMENTS

I would like to thank all the people who supported and guided me through my studies. I would first like to thank my advisor, Dr. Chunqi Jiang, for giving me this opportunity and for guiding me since my undergraduate studies. I would also like to thank my committee members, Dr. Stephen Beebe, Dr. Siqi Guo, and Dr. Michel Audette, for their advice and guidance throughout the course of this thesis and in my academic and professional career.

I would also like to thank my co-workers and friends for their assistance and motivation during the course of this project. In particular, Shutong Song, Johanna Neuber, Steven MacHamer, Brittany Lassiter, and Lucas Potter. I really appreciate all the suggestions and assistance that you gave me and for always being there to bounce ideas off of.

Finally, I would like to thank my family for their never-ending support throughout my graduate career. Without them, this thesis would have never been possible.

TABLE OF CONTENTS

Page

LIST OF TABLES

LIST OF FIGURES

Figure Page

CHAPTER 1

INTRODUCTION AND BACKGROUND

1.1. ELECTROPORATION

The phenomenon of electroporating cell membranes has been an established concept in the medical research field for decades [1]. The idea behind this phenomenon is that a high voltage Pulse Electric Field (PEF), with a varying pulse width, can be applied to a cell and cause its membrane to become permeated (Figure 1). At long pulse widths, in the microsecond range, the PEF is applied to the membrane directly, creating pores in the membrane [2, 3]. However, at much shorter pulse widths, in the nanosecond range, the PEF can bypass the cell membrane and treat the intracellular components, such as the mitochondria and endoplasmic reticulum [2-4]. Difference between the treatment effects caused by these varying pulse widths can be attributed to the plasma membrane charge time. If the pulse width is shorter than the charge time of the plasma membrane, then there will be a higher probability that intracellular components will be treated as well as the cell membrane, since the PEF is able to pass through the membrane.

Whether this effect is permanent is dependent on the total electrical energy applied to the cell. If the energy of the electric field is low enough to avoid permanent damage to the cell, then the membrane will return to normal once the field is removed. This process is known as Reversible Electroporation (RE) and is a novel technique used to introduce substances into the cell that would normally be blocked by the membrane, such as RNA, proteins and drugs [5-7]. When the electric field intensity is high enough to cause permanent damage to the cell, then the membrane will not return to normal once the field is removed, but rather become unstable and eventually lead to cell death. This is known as Irreversible Electroporation (IRE), which is a

commonly used technique in the experimental treatment of cancer cells, including pancreatic, lung squamous cell and breast cancer [8-11].

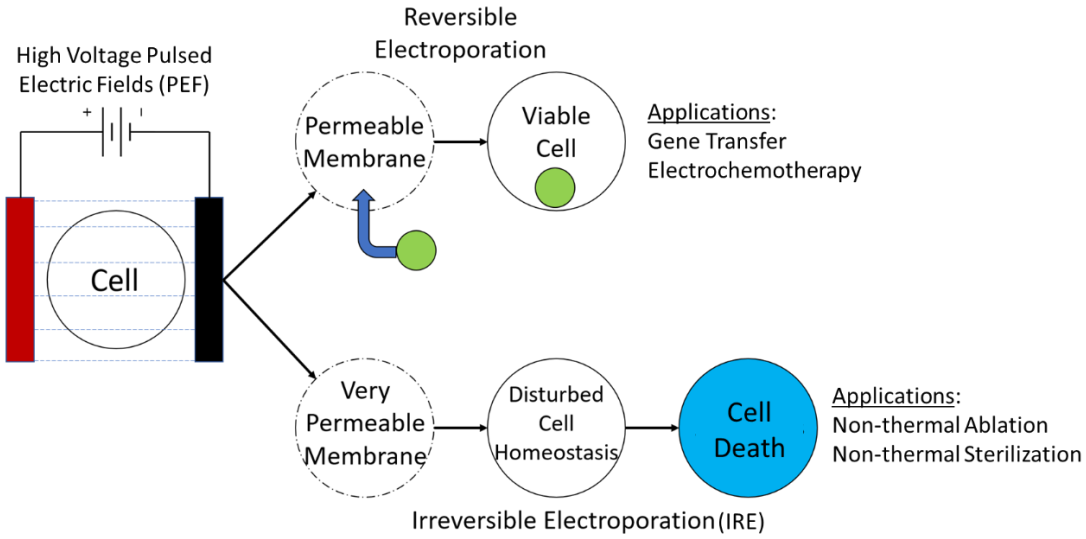

Figure 1: Electroporation overview. Electroporation falls into two categories; reversible electroporation, in which the electric field does not cause permanent damage to the cell membrane and irreversible electroporation, which uses high energy electric fields to disrupt the membrane to the point of eventual cell death.

The application of these PEF is critical in the effective IRE treatment. The most common types of applicators are the needle electrode and the parallel plate electrode (Figure 2). The parallel plate electrode uses two plates of opposite polarities and at a fixed distance to generate a uniform electric field between them (Figure 2). At first, this electrode seems to be the best option to treat tumors because of this uniformity and its non-invasiveness, allowing it to treat cutaneous tumors with ease [12-14]. However, these electrodes are severely limited in the types and sizes

of the tumors they can treat. Parallel plate electrode are ill suited for treating tumors within the body and requires that the tumor size match the dimensions between the plates to prevent electrical breakdown [12].

Needle electrodes on the other hand are not plagued with these issues. They utilize an array of needles at specified lengths and distances apart and apply the electric fields between them. They can treat tumors under the skin as well as larger tumors by using multiple treatment sites [15-17]. Unfortunately, since the electric field is originating from single points, the resulting electric field is non-uniform, as shown in Figure 2. Strongest fields are observed at the needles themselves and become progressively weaker as they move away, which causes the area between the needles to receive a weaker treatment than that of the injection site. Needle electrodes also suffer from frequent surface electrical breakdown issues, since the entire length of the needle is used in the application and it is not uncommon for a portion of the needle to be exposed over the surface of the tumors. This requires that the needles be insulated with some material, such as dielectric gel, to help prevent this type of breakdown. Optimization of these electrodes is critical for IRE treatments of tumors, so a primary goal of this thesis is to find a way to improve a needle electrode so it can mimic the uniformity of a parallel plate electrode.

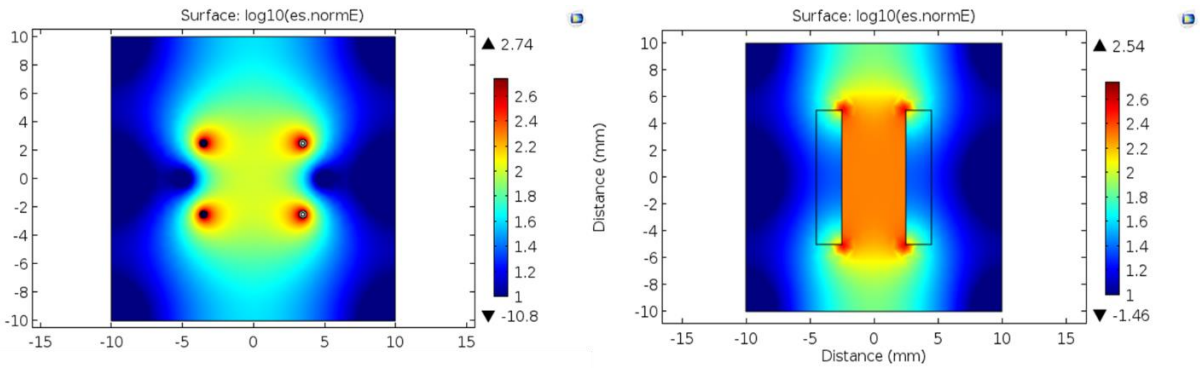

Figure 2: Examples of PEF electrodes. The 4-needle electrode, with a 5 mm x 7 mm orientation, (left) allows for a more generic target size but has a non-uniform electric field distribution between the needles. The parallel plate electrode, with a 5 mm gap distance, (right) has a uniform electric field distribution but it must be tailored to exactly match the target size and can only effectively treat tumors on the skin surface.

1.2. CELLULAR EFFECTS OF MODERATE HEATING

A proposed solution to the non-uniformity issue of the needle electrode is moderate heating. The moderate elevation of temperature, defined as moderate hyperthermia in the clinical sense, has been used in combination with other clinical procedures, such as radiation and chemotherapy, to treat cancer cells [18, 19] (Figure 3). By exposing the body to elevated temperatures of 39 - 45℃ for extended periods of time, > 1 hour, it possible to kill tumor cells with minimal damage to surrounding normal tissue [20]. The reason that the addition of heat is effective at enhancing these treatments is that it effects the fluidity of the cell membrane as well as the homeostasis of the cells as well as denatures proteins, causing cell cycle arrest and inhibition of DNA repair [18, 21-24]. Combination of these cellular effects with the effects caused PEF could prove to have synergistic effects between them, enhancing the overall treatment.

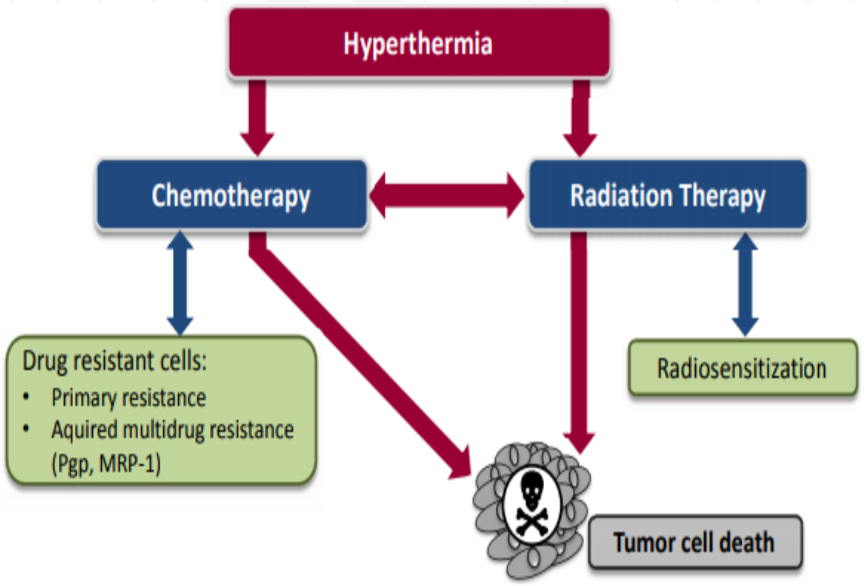

Figure 3: Current applications of heating treatments in clinical setting. The combination of heating in the hyperthermia range with chemotherapy and radiation therapy has shown to improve the elimination of tumors [18].

1.3. MOTIVATION AND HYPOTHESIS

The primary goal of this thesis is to enhance the application of PEF using a needle electrode for treatment of tumors. This will be done by increasing the effectiveness of the needle electrode's PEF through the addition of moderate heating. Based on the characteristics of moderate hyperthermia, we hypothesize that the addition of heat to the regions of weaker field strengths will create a synergistic effect between them, enhancing the overall IRE treatment. Creating a device that can accurately monitor and maintain a specified heat will be integrated into a needle electrode and the thermal effects, such as the change in optical properties of tissue

due to moderate surface heating, will be discussed. This thesis also goes into a detailed analysis of the creation, validation and application of a controlled heating system for use in PEF treatment of pancreatic tumors, which are among the most difficult to treat.

1.4. OUTLINE OF RESEARCH

In Chapter 2, a description of how the device was created including the circuit and electrode design and sensor/optics integration into the electrode as well as the development of the software used to collect the data and control the laser will be given. The characterization of the laser irradiation area using the knife edge technique, observing the changes in the optical properties of pig skin due to prolonged exposure to laser irradiation and *in vitro* studies displaying the synergy between heating and PEF will be discussed in Chapter 3. In Chapter 4, the results of applying this device to PEF *in vitro* and *in vivo* experiments, using pancreatic cancer cell cultures and tumors in mice respectively, will be discussed. And finally, Chapter 5 consists of the conclusion and future work of this device, where the key results found in this study and the future application of this device will be discussed.

1.5. CONTRIBUTION TO RESEARCH

In this project, I was a member of a team performing several biomedical experiments, including nanosecond and microsecond ablation of tumors in mice. My contributions are listed below:

- Controlled Heating System: My primary responsibility was to create the controlled heating system. I designed and constructed the system as well as programmed the user interface in LabVIEW.
- I designed and fabricated the 4-needle electrode used in the experiments
- I performed the characterization of the laser irradiation spot size
- I performed the calibration and validation of the system via the pig skin absorption study
- I assisted in the *in vitro* tests using 3D agarose culture of Pan02 cancer cells
- I participated in the *in vivo* mice experiments, operating the controlled heating system and high voltage pulser in the treatment of pancreatic tumors

Chapter 2

CONTROLLED INFRARED HEATING SYSTEM

In this chapter, the design and fabrication of a device to monitor the temperature of the target sample and controlled the level of heating in real time will be discussed. This overall design process includes selection of an appropriate heat source, the creation of the temperature control circuit, the fabrication of a needle electrode with the integrated optics and electronics, electrical isolation of the smaller voltage electronics, the design of a heating control software.

2.1. HEAT SOURCE SELECTION

There are several options for heating sources that can be used within this device. Some of the more common types of heating sources, which are currently being used in medical and agricultural research, are radio frequency heating, joule heating and laser heating. Radio frequency heating, better known as RF heating, works by applying high frequency (>70 kHz), alternating electromagnetic fields, to a target. The alternating currents applied to the substance causes a volumetric heating effect, the speed and penetration of which is dependent on the applied RF frequency [25]. This process has been used in applications such as food processing and sterilization[25, 26] as well as RF ablation of heart tissue to prevent reoccurring arrhythmias[27]. However, a larger downfall to this technique is that it is notorious for having a non-uniform heat distribution [25] and the high frequency electromagnetic fields would severely affect the small scale electronics in the system. These criteria make RF heating ill-suited for this application.

Joule heating, also known as ohmic heating, uses the passage of electric current through a resistive material to produce heat [28]. This is seen on practically at electronic devices, often requiring them to have heat sinks or fans to prevent temperature damage to the circuitry. This type of heating has been used in food processing by using high energy PEF [29] but this high energy requirement is dangerous to apply safely in a clinical setting, making ill-suited for this application. Using this type of heating would also require altering the pulsing parameters of the IRE treatment, making it not relatable to other studies.

The last option, laser heating, uses high intensity laser light to heat the surface of the target. The wavelength of this laser light helps determine how deep it can penetrate the tissue, with longer wavelengths having further penetration [30, 31]. The overall intensity of this surface heating as well as the distribution of the heating can also be altered by either changing the distance between the laser fiber and the surface or by manipulating the light using lens, allowing for fine control of the heat distribution. Since this type of heating only uses light, it has little chance of indirectly interfering with other electrical devices in the system. Finally, the optical fibers that deliver this laser light can be easily integrated into an electrode. Based on these criteria, laser surface heating was chosen as the heating source for this device.

The laser system used in this study was purchased from Lasermate Group Inc. This Class 4 Laser Power Supply operated at 980 nm and with a peak power <8 W. This wavelength was chosen based on the success of previous studies using this condition, including laser assisted gene therapy[32] and a comparison study using Bovine tissue[30]. The laser power was adjustable and the laser status could be controlled manually or with a TTL signal from a computer, allowing for autonomous control. The fiber used to deliver this laser light, purchased from Thor Labs, was a M79L005 980-nm optical fiber. During the calibration tests, the laser was

measured using a power meter and once an optimal setting for the experiments was found, the laser energy was kept constant in all *in vitro* and *in vivo* studies.

2.2. TEMPERATURE CONTROL CIRCUIT

The key aspect to this controlled heating system is the sensor itself. Since it will be used in high electric fields and during biological experiments, it is required to be non-invasive, highly accurate and high voltage safe. It also needs to be able to read the heat from the surface of the target correctly even when the laser is on and not be effected by the wavelength of the applied laser irradiation, 980-nm. With these requirements in mind, the ZTP-135 thermopile sensor was chosen for its ability to read infrared signals at the target surface with high precision, its built-in ambient temperature compensation through a thermistor and it does not detect the laser wavelength [33].Thermopile sensors have been used in many projects for remote temperature measurements, including remote temperature sensing of human body temperature [34, 35], making it an ideal choice for this project. The modified circuit diagram used for this device is shown in Figure 4.

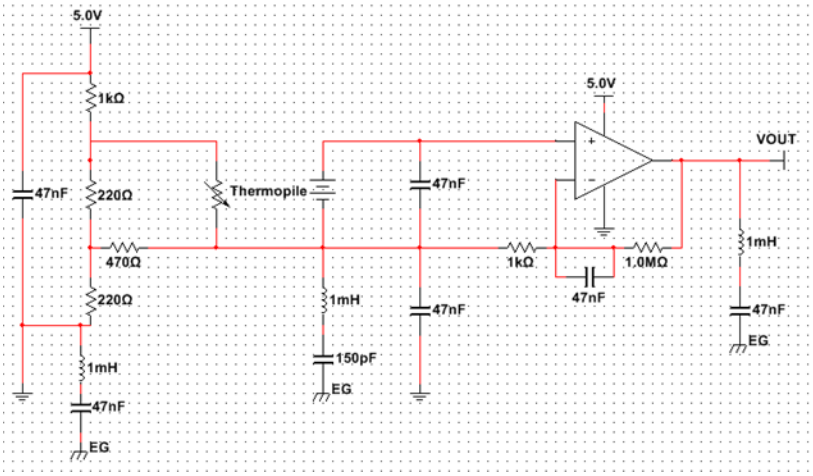

Figure 4: Modified thermopile temperature measuring circuit. An Arduino Uno microcontroller was used to power the circuit and collect the voltage readings from V_{out}. This circuit design is based on the original patent [36], and was modified to accommodate for the electrical noise seen by the PEF. Addition of three low-pass filters, a 400-kHz filer connected directly to the thermopile and 24 kHz filters attached to the Arduino board connections were used to prevent electrical interference and damage from the PEF treatment.

The thermopile works by converting the thermal energy from the target into an electrical energy, in the millivolt range, while the thermistor uses the thermal energy to determine its resistance, both of which can be translated into a temperature reading. The purpose of the thermistor is to help compensate for the surrounding temperature signals and reduce the error of the thermopile readings. The complete compensation of the surrounding temperature is handled by a combination of $R1 - R4$ and the thermistor, which minimizes the error in temperature detection by creating a reference voltage V_{ref} [36]. The thermopile sensor's output, $V_{thermopile}$, is amplified in the non-inverting output of the operational amplifier while the reference voltage is applied the inverting output. The output voltage signal, V_{out}, is determined by the following expression:

$$V_{out} = V_{thermopile} * \left(1 + \frac{R6}{R5}\right) + V_{ref} \quad (1)$$

Where, $\left(1 + \frac{R6}{R5}\right)$ is the amplifying ratio of the operational amplifier.

This circuit utilized a amplifying ration of x1000, which allowed the Arduino to accurately read the thermopile readings. The output voltage, ranging from 0 to 5V after amplification, is supplied to the Arduino Uno microcontroller's Analog to Digital Converter (ADC), which converts this voltage signal into a digital signal that can be calibrated into a temperature reading. As an initial test of the circuit's functionality, a calibration was performed using a heat block and an external thermometer as a reference. The thermopile was fixed at the optimal field of view angle of 90° to the target surface and at a varying distance between 1 cm and 5 cm away from the eat block surface. Starting at room temperature, the heat block was heated to 50°C. At each 1°C increase in temperature, the digital value displayed by the Arduino was assigned the temperature value specified by the thermometer. Once the heat block reached 50°C, it was turned off and this procedure was repeated as it returned to room temperature. The set-up for this experiment is shown in Figure 5.

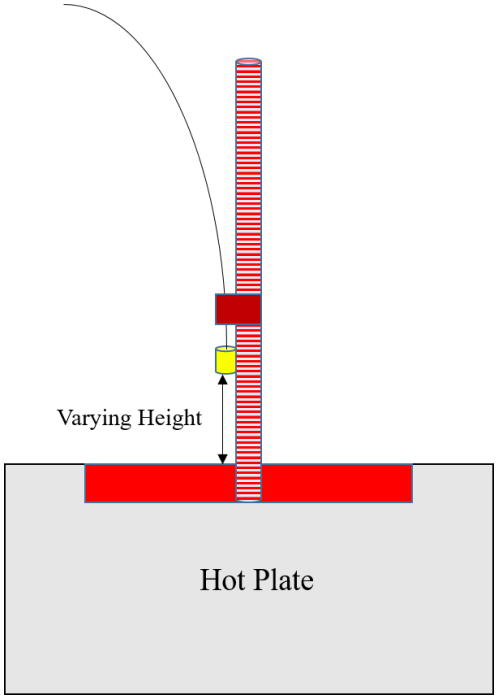

Figure 5: Thermopile calibration using a heat block. The thermopile was placed at varying distances away from the heat block surface and the temperature trend over time was measured and compared to that of the thermometer and thermocouple to confirm the accuracy of the device.

This trend data was fitted with a linear fit and the calibration equation that could convert the digital ADC signal from the Arduino to a real temperature measurement was created. This calibration was performed for a thermopile distance of 1 – 5 cm, in 0.5 cm increments, and a total of 3 heating and cooling measurements were taken at each different distance. The calibration equation for each height was the result of averaging the heating and cooling trends together. The results of this calibration is shown in Figure 6.

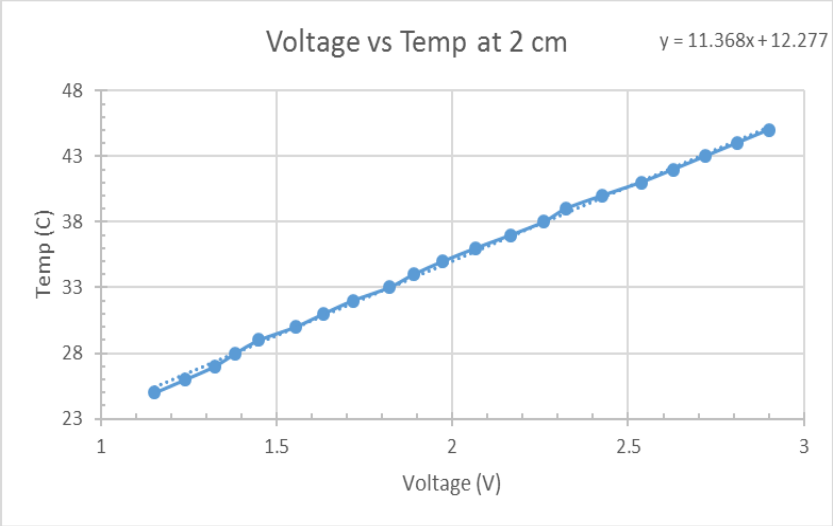

Figure 6: Heat block calibration results. Left: This trend is the result of averaging 3 room temperature to 50℃ measurements and three 50℃ to room temperature measurements. It was determined that small changes in distance (±1 cm) between the thermopile and target surface had little effect in this orientation.

Another issue that needed to be addressed was the electrical noise caused by the high voltage PEF. Since the thermopile device works in the millivolt range, it can pick up small amounts of noise generated from the PEF, resulting in large temperature reading errors. To ensure high voltage safety and electrical noise protection for this circuit, several low-pass filters were implemented. The filter attached directly to the thermopile has a cutoff frequency of 410 kHz while the filters added directly to the reference voltage circuit and the output voltage has a cutoff frequency of 23 kHz. These filters were grounded to the metal enclosure that encased the circuit and microcontroller, which acted as a Faraday Cage and isolated the small voltage electronics from the high voltage fields that were being used. In addition to the metal casing, the wires connected to the thermopile were shielded using a French braid shield, which was terminated to

the metal enclosure, effectively isolating the entire device from external electrical noise. The completed control circuit, including the isolation box, is shown in Figure 7.

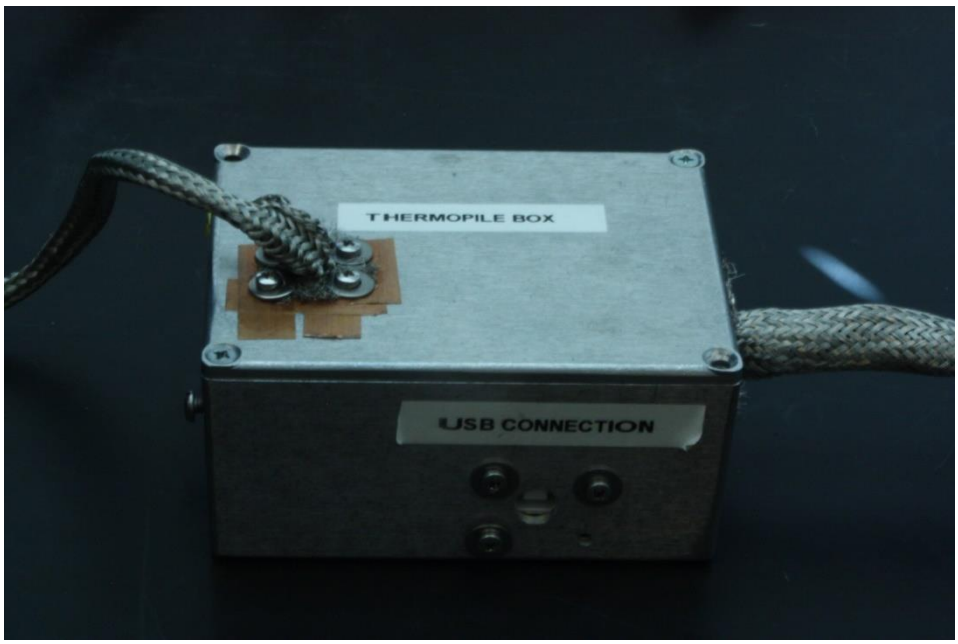

Figure 7: Completed control system for surface temperature monitoring and laser control. The box contains the control circuit and the Arduino Uno. All external connections are shielded using French Braid ground cable, including the external thermopile wires, BNC connection to the laser poser supply and the USB connection from the Arduino Uno to the computer.

2.3. ELECTRODE INTEGRATION

The next step was to integrate the thermopile and laser fiber optics into a 4-needle electrode. The electrode was constructed from a Polytetrafluoroethylene (Teflon; PTFE) cylinder, which is known for its high voltage resistance and ease of machinability. The needles used to apply the

electric fields were 25-gauge hypodermic needles that were oriented in a 5 mm x 7 mm orientation, where the like charges needles were 5 mm apart and the oppositely charged needles were 7 mm apart, with a length of 1.5 cm from electrode base to needle tip. These needles were insulated using ETFE (Ethylene tetrafluoroethylene) tubing that extended from the internal connections between the needles and supply cables to a set distance away from the tip of the needles. The exposed portion of the needle could be easily adjusted based on the size and depth of the target, allowing for a more generalized application. Additional insulation provided by theses sleeves not only increased the electrode's peak voltage capability but also reduced the occurrence of local breakdown during treatment since the exposed needle length could be tailored to the target thickness, preventing deep needle penetration and exposed needles above the injection site. This also allowed for the use of longer needles, which allowed the user to visibly see the injection site during treatment and react more effectively to experimental changes, such as local breakdown.

A 980-nm laser optical fiber was placed within the center of electrode and flush to the electrode surface, targeting the laser light at the weakest portion of the electric field. The thermopile was integrated into the side of the electrode, which allowed it to observe the center of the 5 mm x 7 mm needle array where the laser was focused, using the diagram shown in Figure 8. However, using this side orientation reduces the efficiency of the thermopile readings based on the severity of the field of view angle, θ.

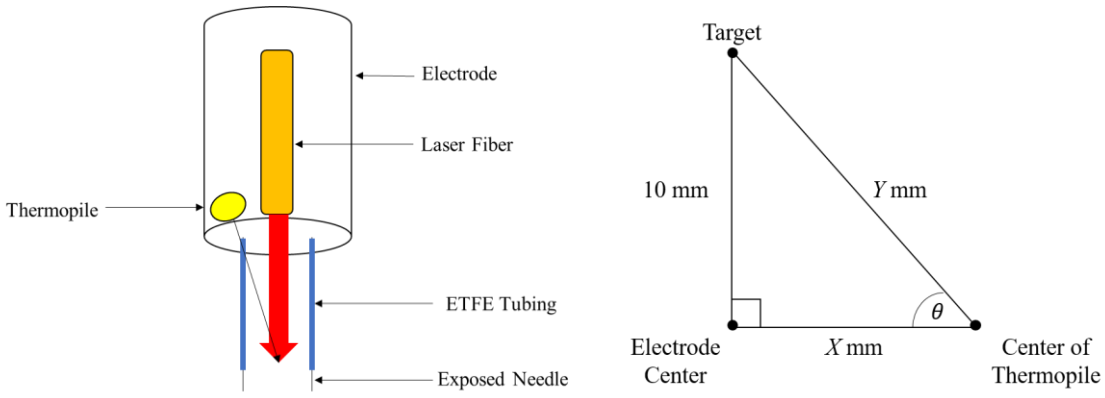

Figure 8: Electrode conceptualization. The laser fiber is integrated within the center of the electrode while the thermopile is integrated to the side, angled to observed the laser treated area (left). The value of this angle is determined by the physical properties of the electrode and the shielded needle length (right)

When designing the integration angle for the thermopile, the goal was to get the highest efficiency possible within the physical limitations of the electrode. Limitations such as the shielded needle length, which accounted for the distance between the electrode and target during treatment, the center-to center distance between the laser fiber optic and the thermopile, *X*, and the thermopile diameter, the size of the hole that needed to be drilled, where take into consideration. Using these parameters and geometry of a right triangle, the angle of the thermopile's field of view can be calculated. The final design used a shielded needle length of 1 cm and 5 mm center-to-center distance between the thermopile and laser fiber optics, creating field of view angle of 27.5°, which reduces the efficiency of the thermopile to 60% [33].The finalized electrode is shown below in Figure 9.

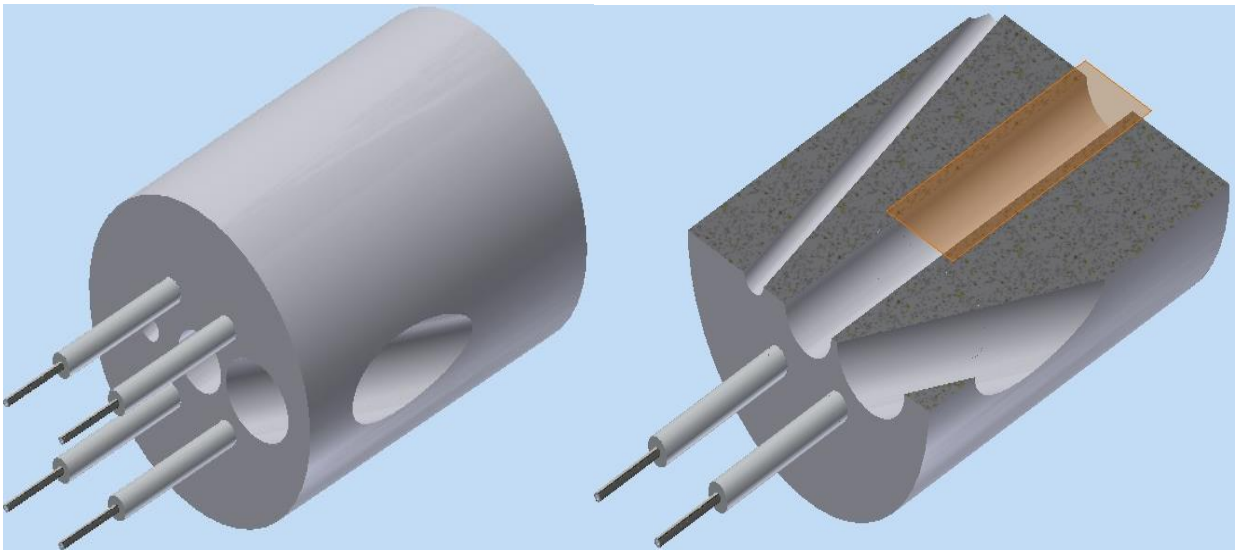

Figure 9: Electrode AutoCAD schematic. The final electrode is a 5 mm x 7 mm 4-needle Teflon electrode with three slots drilled into it. The center slot houses the laser fiber, the left slot houses a fiber optic temperature sensor used for calibrations and the right slot houses the thermopile

Using the completed electrode device, a calibration test was performed using a pig skin sample as the target and an external thermocouple to validate the temperature readings seen by the thermopile, to ensure that the device was working properly. A simple control program was created in Arduino to control the status of the laser based on the temperature reading provided by the thermopile. If the reading was higher than the preset target, then the laser would be turned off. If the reading was lower than the preset target, then the laser would be turned on. In the case of this calibration, the temperature target was set to 43℃, which is the target temperature required in many of the studies this device would be involved in [23]. The overall set-up and results of this calibration are shown in Figure 10.

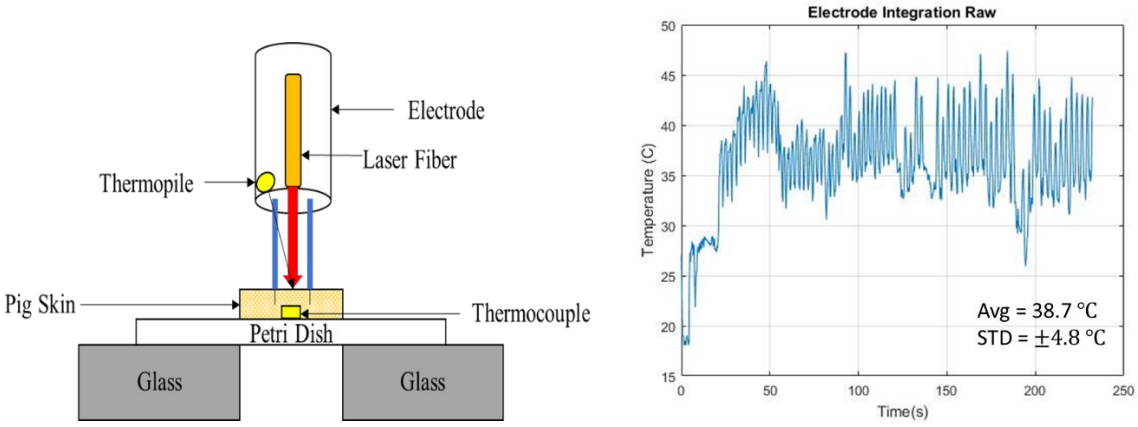

Figure 10: Initial electrode calibration set-up and results. Using the custom electrode and a simple control program, the pig skin sample was heated to a target temperature of 43°C using the laser and monitored by the thermopile and an external thermocouple in real time (left). The result of this test showed that the orientation of the thermopile has a significant effect on the system's ability to maintain a specified temperature (right).

Unfortunately, as shown above, the first attempt at the calibration was largely unsuccessful. This was mainly due to the thermopile's field of view within the electrode. The side orientation of the thermopile may allow the thermopile to read infrared signals directly at the laser/tissue interaction site but it severely reduces the efficiency of the readings, since the optimal field-of-view angle of the thermopile is 90° to the surface. Even at 60% efficiency, a detrimental effect is clearly seen during the initial calibration of the device and prevents it from even reaching the target temperature of 43℃. Rather than redesign the electrode to better suit the thermopile, we decided to explore a programable solution to this problem.

2.4. OVERSAMPLING AND AVERAGING

As stated before, the Arduino Uno uses an ADC to read and convert the signal from the thermopile to the computer display. This is done by relating a range of voltage values, or an analog signal, to a range of digital values that can be read by a computer, which can then be calibrated to represent a desired reading, such as temperature. The resolution of this reading is heavily dependent on the range of digital values that the ADC can produce, known as the bits of resolution. The range of digital values that the ADC can resolve is determined by the following equation:

$$number\ of\ discrete\ value = 2^{bits\ of\ resolution} \quad (2)$$

In the case of the Arduino Uno, a 10-bit ADC is provided, allowing it to produce a range of 1063 digital values for the ADC to assign data values to and the ability to resolve voltage changes as small as 5 mV in a 5 V range [11],which produces the results shown in Figure 10. The only way to get a better signal is to either improve the quality of the signal, which would mean redesigning the electrode, or use a higher resolution ADC to resolve the finer changes in temperature, which would also help compensate for the lower efficiency. Since the Arduino's ADC is built-in and hooking up a higher resolution ADC would not only cause slower readings but would be much more expensive, we decided to apply a programming technique known as oversampling to the data collection.

Oversampling is a process by which a set number of samples are taken at a lower resolution and averaged together to create a single sample at a higher resolution [37-39]. The number of samples needed to be collected and averaged is determined using the following relationship:

$$Samples\ needed = 4^{(Desried\ bts)-(starting\ bits)} \quad (3)$$

For example, if you wanted to increase your ADC from a 10-bit resolution, which has 1023 discrete levels it can use to label temperature readings, to a 12-bit resolution, which has 4096 discrete levels it can use to label temperature readings, you would need to collect and average a total of 16 data points at the 10-bit resolution to get one point at the 12-bit resolution. The increased resolution of this processing technique is shown in Figure 11 [38].

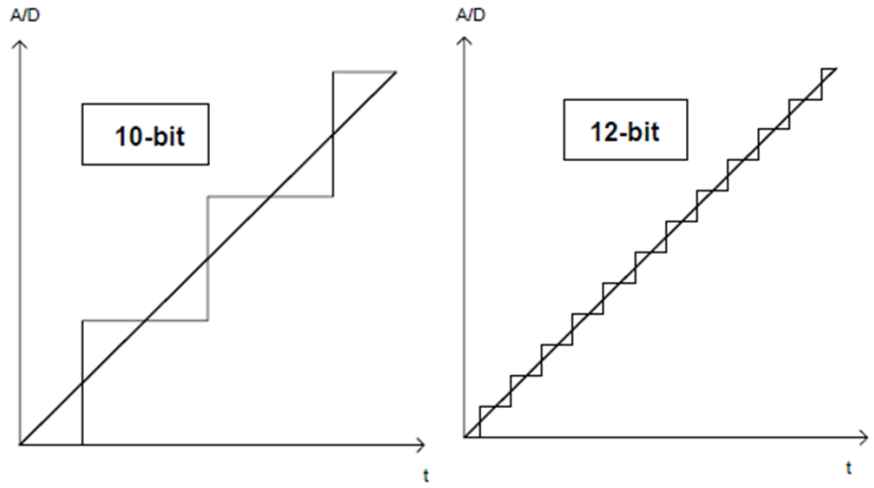

Figure 11: Oversampling resolution increase example. The resolution of an ADC determines how the fine the voltage resolved data is. Higher bits of resolution results in are more discrete levels that the voltage can be assigned to, resulting in smaller changes in voltage being resolved [38].

By using this process, we not only mimic a higher resolution ADC, which can resolve finer changes in voltage, but we are also averaging many samples to do so, which would reduce the

error of the readings caused by the reduced efficiency. However, this process has one large drawback, the sampling speed. As the gap between the desired and original ADC resolution gets larger, significantly more samples at the lower resolution are needed to create the single sample at the higher resolution, which results in reduced sampling rates. The actual limit of the sampling speed varies depending on the microcontroller being used. In the case of the Arduino Uno, the different requirements for increasing the 10-bit ADC to higher resolutions are shown in Table 1.

Table 1: Arduino Uno oversampling statistics [11]

Over-sampled Resolution	Additional Commanded Bits of Precision, n	Voltage Resolution (for 5V Arduino) (mV)	# 10-bit Samples Required to Achieve this Resolution, $S_{10\text{-bit}}$	Time per Reading at this Resolution (sec)	Nyquist Freq[1], f_{Nyq} (Hz) (ie: this is the max. frequency that can be detected, via sampling, w/out aliasing, based on your sample rate)
10 bit	0	4.8876	1	0.000120482	4150.000 Hz
11 bit	1	2.4438	4	0.000481928	1037.500 Hz
12 bit	2	1.2219	16	0.001927711	259.375 Hz
13 bit	3	0.6109	64	0.007710843	64.844 Hz
14 bit	4	0.3055	256	0.030843373	16.211 Hz
15 bit	5	0.1527	1024	0.123373494	4.0527 Hz

The maximum possible sampling rate that the Arduino can reliably achieve at 10-bits is about 4 kHz. As the resolution of the ADC increases, this sampling rate begins to drop rapidly, being reduced by a factor of about 4 from just increasing the resolution by 1 bit. Based on this trend, oversampling at resolution of 15-bits was chosen because it not only provided ~33000 discrete values to assign temperature values but it still allowed for a sampling rate of 4 Hz, which was

more than enough to monitor and maintain the laser heating in real time. This improved ADC was tested using the sample calibration set-up as before (Figure 10) and was able to reach the target temperature of 43℃ with a standard deviation of ±1.8℃, shown in Figure 12.

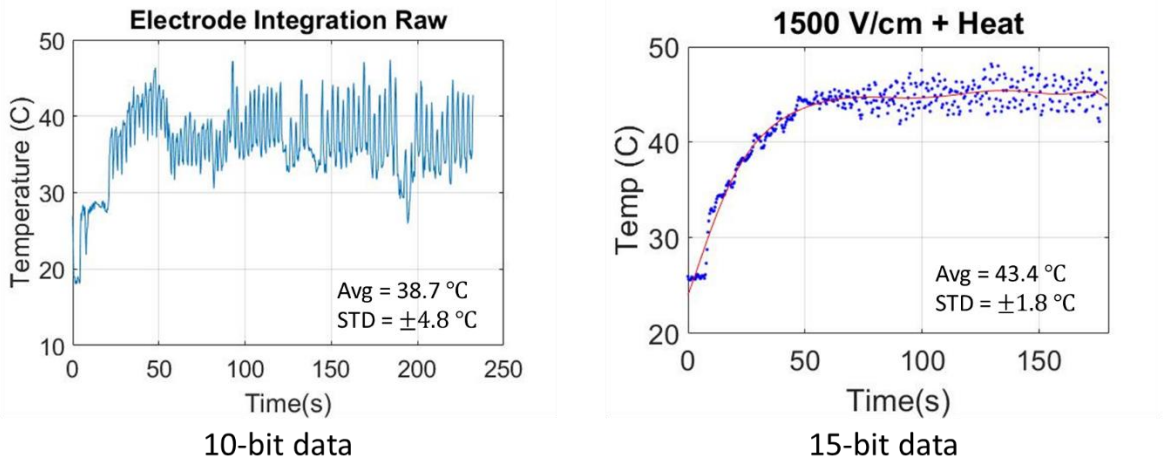

Figure 12: ADC resolution comparison. Repeating the calibration test from Figure 10, a target temperature of 43°C was set in the program using a 15-bit ADC resolution. The 10-bit resolution (left) was unable to maintain the desired value while the 15-bit resolution (right) could maintain this value with a standard deviation of ±1.8°C.

2.5. LABVIEW GRAPHICAL USER INTERFACE (GUI)

With the electrical and mechanical components completed, the final step was to create an effective and user-friendly interface that could control this system. LabVIEW was chosen as the platform due to its ability to communicate effectively with the laser, through TTL signaling, and the control circuit, through a VISA resource to the Arduino Uno, as well as its interface capabilities. The current version of the LabVIEW GUI is shown in Figure 13.

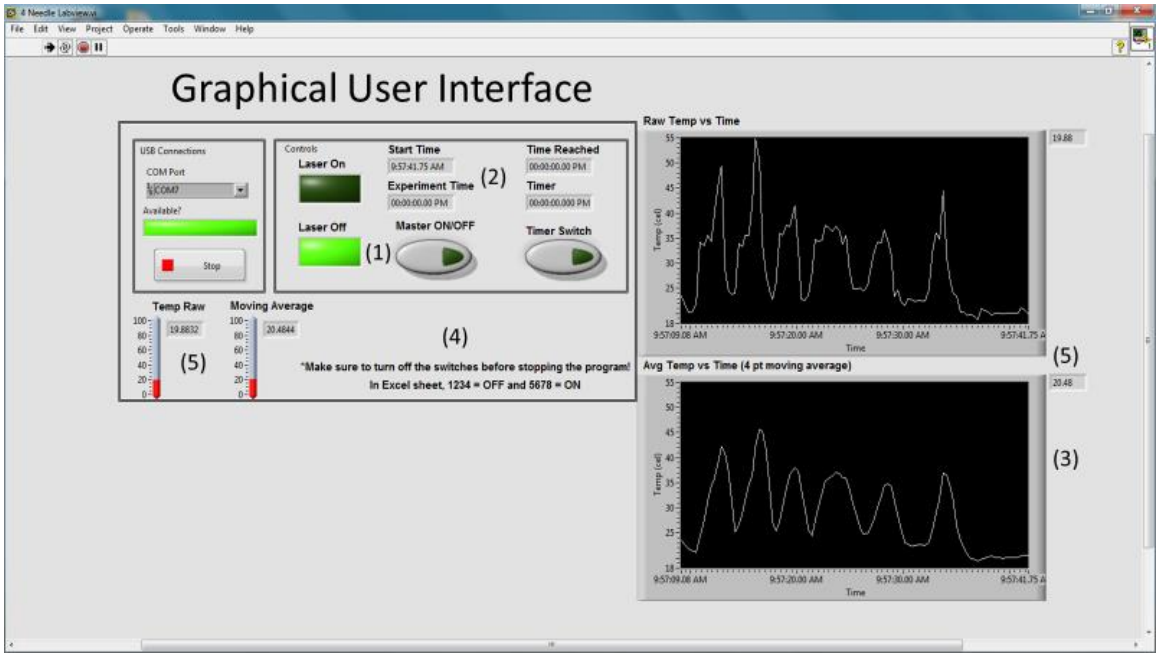

Figure 13: LabVIEW Graphical User Interface (GUI). 1) Manual and automatic control of the laser. 2) Time logs of total heating time, pre-heating timing, total experiment time and an extra timer used for laser control. 3) Oversampled and averaged data, which controls the laser. 4) Automatic storage of all data including time dependent laser status, temperature data and all times specified. 5) Monitoring of uncorrected data for error checking, since the oversampling and averaging data correction would mask errors.

The current iteration of this interface sports many essential and useful functions. By far the most important is the updated feedback loop between the thermopile and the GUI. Before, this process was performed solely with the Arduino Uno and was limited in its ability for user interactions. Using this GUI, the feedback system can now be controlled and manipulated as the user sees fit, using switches or timers to prevent laser heating in accordance with real treatments. This GUI also implements the oversampling correction to the data received and uses it to control the laser automatically. Finally, this interface allows for real time storage of the data including

when the laser was ON/OFF, the display and collection of the uncorrected and corrected data and all timing involved with the heating protocol including total heating treatment time, preheat time, total experiment time and laser control timer, which allows the user to stop the laser for a set amount of time without stopping the program.

2.6. FINAL PRODUCT

The final system consists of a custom designed 5 mm x 7 mm 4-needle electrode with an integrated 980-nm optical laser fiber and ZTP-135 thermopile temperature sensor. These fibers and sensors operate in real time to monitor and maintain a specified surface temperature. The LabVIEW generated GUI allows the user to observe the temperature trend data over time and performs data corrections, though oversampling, to increase the accuracy of the readings. Other functions of this interface include manual laser control, monitoring of significant heating events and real-time storage of all heating data. Overall, this system can maintain a target temperature at an accuracy of $\pm 1.8℃$ before and during the application of PEFs with little to no electrical interference.

Chapter 3

THERMAL NALYSIS OF LASER IRRADIATION

In this chapter, the characterization of the laser spot size using the knife-edge technique, a study of the effect that laser irradiation heating has on the optical properties of pig skin and an *in vitro* study to display the synergistic effects of the combined treatment protocols is presented. Understanding these effects caused by laser heating will provide valuable insight into how the device affects cells and tissue as well as help to create a heating protocol for future *in vitro* and *in vivo* experiments.

3.1. LASER SPOT SIZE CHARACTERIZATION

This section presents an in-depth analysis of the laser irradiation spot size is performed via the knife-edge technique. Even though the definitions of a Gaussian laser beam are well defined, it becomes challenging to characterizing the spot size using the equations alone. It is impossible to know the specific properties of a beam, such as the nature of the laser light and the beam structure, without physically measuring them. This information is vital in characterizing the power distribution area that the optical fiber can provide, which will determine the effective area of heating.

3.1.1. Characterization options

In general, the 2D power distribution of Gaussian beam is characterized using the following equation [40]:

$$P(x,y) = I_0 \exp\left[-\frac{2 * ((x-x_0)^2 + (y-y_0)^2)}{r^2}\right] \quad (4)$$

Where, I_0 is the initial laser intensity and r is the $1/e^2$ radius of the beam.

An increased laser irradiation area allows for an easier penetration of heat into the tissue. The accurate measurement laser beam profile is very important in this controlled heating system. There are many techniques available to perform this analysis, including the slit scan technique [41], the pin hole technique [42], and the knife edge technique [40, 43, 44]. The pin hole technique uses an autonomous system to analyze the laser irradiation at every point within the beam by scanning a small opening across the beam. While this would create an extremely accurate representation of the profile, it would take a substantial amount of time and specific equipment to create this system, making it not ideal for this application. On the other hand, the slit and the knife edge technique are much simpler to perform and work using the same principle, traversing the laser beam across the knife edge/slit and record the energy of the beam that is unobstructed. This allows for a quick, inexpensive and, more importantly, accurate representation of the cross-sectional area of the laser. For this thesis, the knife edge technique was utilized.

As previously stated, the knife edge technique uses a razor-sharp knife edge and is moved it in micrometer increments perpendicular to the beam propagation and the total transmitted power, measured with a power meter, is measured in relation to the position of the knife, as shown in Figure 14.

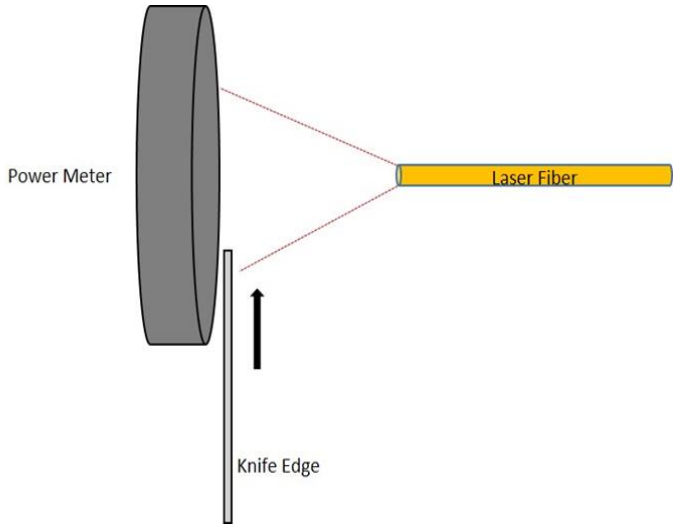

Figure 14: Beam profile experimental set-up. The laser fiber was set at 1, 1.5 and 2 cm away to determine the optimal distance within the electrode. In all cases, the data was collected in triplicates.

As the knife moves across the beam, the laser energy will start to decrease until the beam is completely obscured by the knife, as shown in Figure 15. This plot shows the 2D Gaussian profile of the beam integrated over the displacement of the knife edge [40]. In order to find the radius of this beam, normally defined as the $1/e^2$ radius for gaussian profiles, a smoothing derivative is applied to the collected data (Equation 5) and fitted with a 1st or 2nd order gaussian trend line depending on the type of laser, also shown in Figure 15.

$$\frac{dP_T}{dx} = \frac{1}{2}\left(\frac{y_{i+1} - y_i}{x_{i+1} - x_i} + \frac{y_i - y_{i-1}}{x_i - x_{i-1}}\right) \quad (5)$$

Using this fit, the $1/e^2$ radius can be determined by measuring the distance between the points corresponding to 13.5% of the peak power value.

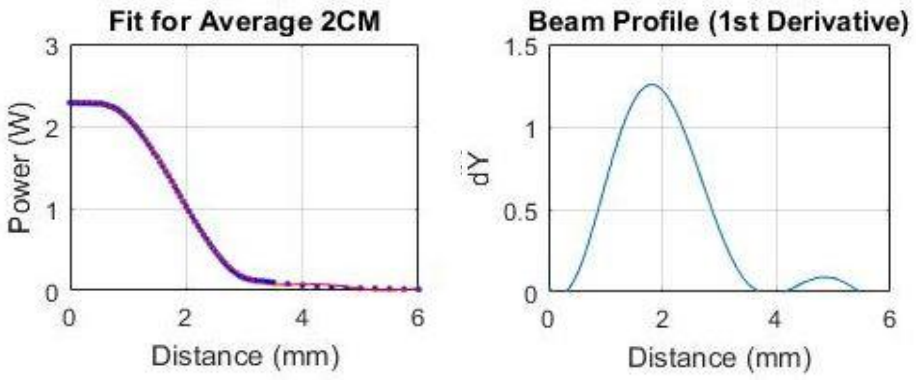

Figure 15: Ideal gaussian beam profile and data collection. The image on the left shows the data collected by moving a knife edge across a laser beam in 5 µm increments. The image on the right shows the smoothing derivative of the data, which can be used to determine the width of the beam

Using the knife edge technique, it is possible to determine the optimal position of the fiber within the electrode that would allow for the largest area of coverage very quickly and easily, making it the optimal choice for this experiment.

3.1.2. Materials and methods

The set-up for this procedure is shown in Figure 14. The knife edge technique was performed at varying fiber distances to achieve the greatest laser irradiation area. However, due to the geometry of the electrode, the laser fiber could only be place at distance between 1-3 cm away from the surface, flush to the surface of the electrode and at the end of the housing respectively. With this constraint in mind, this test was performed for 1-3cm fiber distances in 0.5 cm increments. These tests were performed with the laser fiber inside the electrode. Since the input laser power ultimately determines what the peak intensity is and liminality affects the laser

distribution, it was kept constant at 2.31 W. The determination of the optimal laser energy will be discussed in Section 3.2.

3.1.3. Results and discussion

Based on the results shown in Figure 16, the distance between the laser fiber and the target plays a significant role in the distribution of the laser irradiation. At a close distance, 1 cm between the fiber and power meter, a high intensity, narrowly focused beam is observed. This would cause significant heating at the center of beam but very limited heat distribution to the surrounding tissue. As the distance between the power meter and laser increases, the laser spot size becomes larger while becoming less intense. At a of 2 cm, the spot size of the beam was observed to be a factor of 2.92 larger than that of the 1 cm condition but at a peak intensity a factor of 2.62 less than the 1 cm condition. These data values are shown in Table 1.

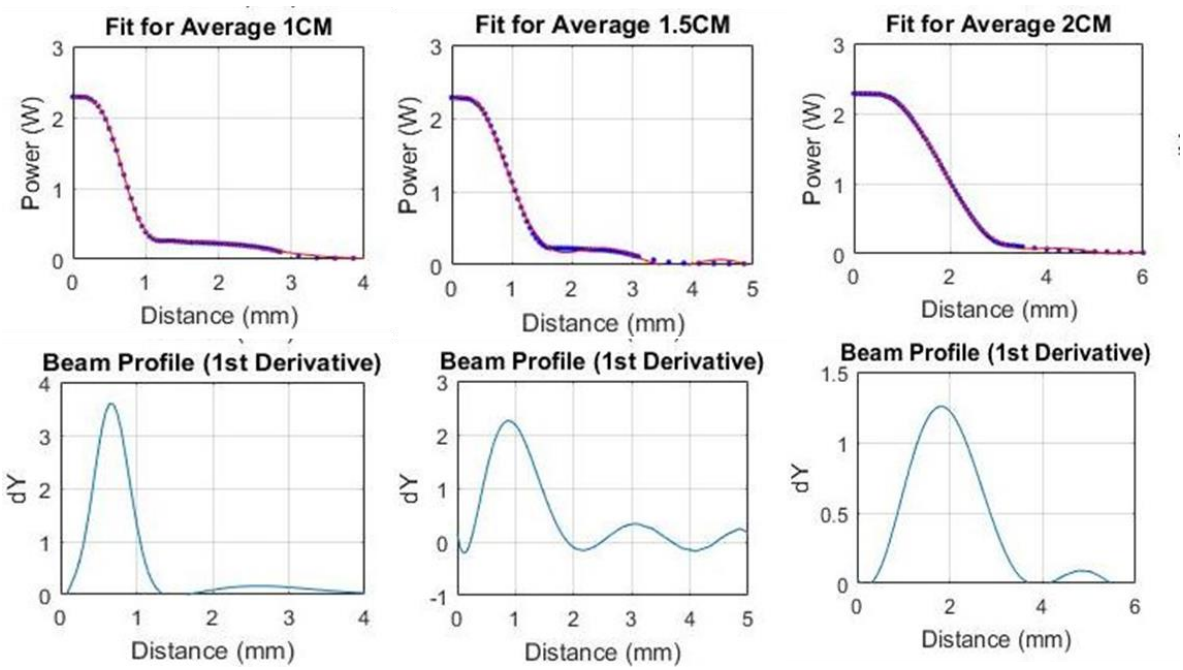

Figure 16: Beam profile results at varying distances. Each prolife represents an average of 3 separate datasets with an error of ±0.05W and fitted with a 2nd order gaussian trend line using MATLAB's curve fitting toolbox.

Table 2: Measured beam widths and peak irradiation values at varying distances

Distance (cm)	1/e^2 Radius (mm)	Peak Irradiation (a.u.)
1	0.925	3.62
1.5	1.42	2.31
2	2.71	1.38

It was observed that fiber distances greater than 2 cm would result in a truncated beam. This is due to the opening provided in the electrode for the laser fiber, which was made to the exact size of the outer diameter of the fiber, to ensure the fiber stayed in a constant position. While increasing the fiber distance is still possible, and would result in a similar heat distribution to 2 cm but with high intensity values, it was still not an ideal option because the electrode would be heated. This would not only be unsafe for the person using this electrode but it could also damage the components within the electrode and effect the thermopile readings.

In addition to the spot size and peak irradiation comparison, a 2D comparison of the laser irradiation distribution at these distances was performed. When translated to a 2D profile, is was clear that a fiber distance of 2 cm away from the target was ideal for this set up since it would cover almost the entire central area of the electrode. This orientation would allow the deposition of heat to be more uniform across the central region where the electric field is weakest, as shown in Figure 17.

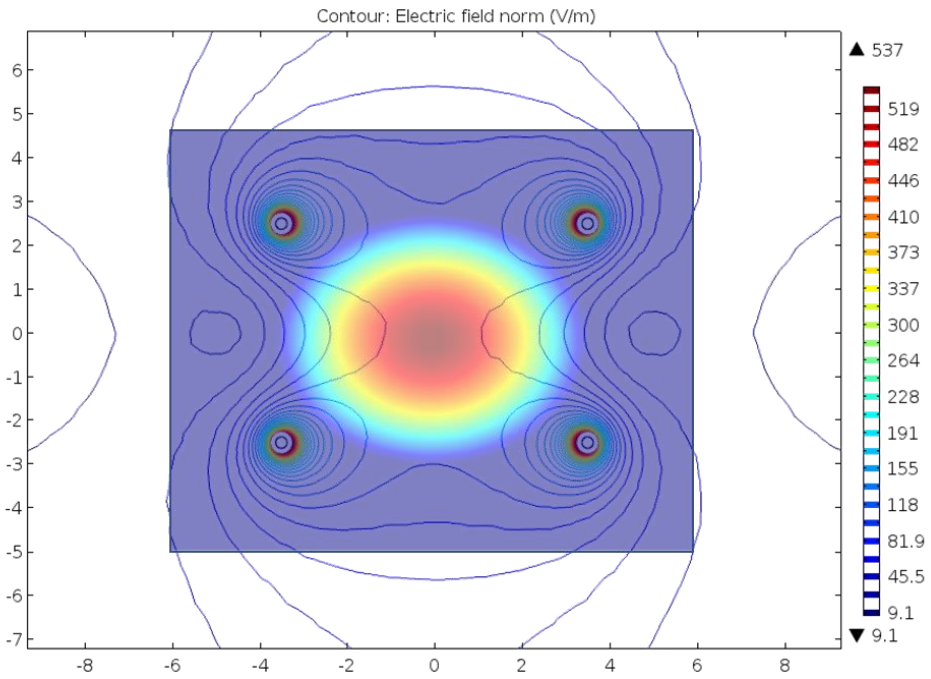

Figure 17: Proposed synergy between laser irradiation and PEF of 4-needle electrode. 2D beam profile at a fiber distance of 2 cm. Beam profile data was normalized after applying a logarithmic scale. The electric field was simulated in Comsol Multiphysics using the geometry of the 4-needle electrode and the electrostatics physics module.

Completion of this test showed that 2 cm between the laser fiber and the target surface is the maximum this electrode orientation would allow without truncating the beam and would provide an irradiation area of about 6 mm^2, which adequately covers the central region of the electrode. Analysis of the penetration depth will be discussed in the next section.

3.2. OPTICAL CHANGES IN TISSUE CAUSED BY THE LASER

The purpose of this study was to analyze the effects the laser heating would have on the optical properties of sections of pig skin, such as absorption and heat diffusion depth. Knowledge

of these effects will allow for optimization of the laser parameters for future *in vivo* and *in vitro* treatments as well as provide an idea of what the laser heat diffusion would look like, which would determine if the laser spot size needs to be increased.

3.2.1. Laser tissue interactions

To quantify the effects that the laser heating treatment would have on tissue, calibration tests were performed with harvested pig skin, due to its similarities to human skin [45-47]. Specifically, the penetration depth of the laser and the amount of heat that diffused through the tissue over time were measured through observing the changes in the optical properties of the sample. When light hits the target sample, a portion of it is scattered, absorbed and transmitted further into the sample [31]. Scattering of the laser light takes place when the direction of propagation of the photons changes. This causes the light to spread out in all directions, which in turn limits the depth of penetration. Transmission of the laser light, which determines the penetration depth of the heating, is dependent on the material it is interacting with as well as the wavelength of the light. Typically, the longer the wavelength of light, the deeper it can penetrate the tissue. Scattering and transmission of the light accounts for only a small portion of the total signal. Most of the light is absorbed by the tissue sample, which generates the desired heating effect. However, this occurs mainly at the surface of the tissue and slowly diffuses down.

The key to making this heating effective is not only to maintain a specific temperature but to also ensure it is a uniform temperature throughout the target area. The goal of this study is to examine the effect that prolonged laser exposure has on the absorption property of the tissue, which can shed light on how long the tissue sample needs to be exposed to allow for more penetration of laser light deeper into the tissue, creating a deeper heating. By observing the

amount of laser light transmitted through the sample with a power meter, properties such as the absorption coefficient, scattering coefficient, the effective penetration depth of the laser could be found analytically [48, 49]:

$$\frac{I_S}{I_0} = e^{-\mu_t d} \tag{6}$$

$$\mu_a = -\left(\frac{2.303}{d}\right) * ln\left(\frac{I_S}{I_0}\right) \tag{7}$$

$$\mu_t = \mu_s + \mu_a \tag{8}$$

$$\delta = \frac{1}{\sqrt{3 * \mu_a * [\mu_a + \mu_s(1-g)]}} \tag{9}$$

$$g = 0.62 + 0.29 * 10^{-3} * (\lambda_{laser}) \tag{10}$$

Where, I_s is the transmitted light through the sample, I_0 is the initial light intensity, μ_t is the total attenuation coefficient, *d* is the thickness of the sample, μ_a is the absorption coefficient., μ_s is the scattering coefficient, λ_{laser} is the wavelength of the laser, δ is the effective penetration depth of the laser and g is the average cosine angle of scattering, which can be assumed using this relationship shown in Equation 10 [49].

3.2.2. Materials and methods

3.2.2.1 Pig skin harvesting

The pig skin was harvested from euthanized pigs from other biological experiments by the vivarium staff in the Center for Bioelectrics and was kept frozen at $-20℃$ for preservation. Before each test, a large sample was thawed to $20℃$ using a warm water bath and then was sectioned off in to appropriate sized pieces using a scalpel. The smallest sections of pig skin (~3 mm) had a minimal hypodermal layer on them, leaving primarily the dermis and epidermis. Any sample larger than this size is a result of a larger hypodermal layer of tissue. These varying thicknesses were chosen to analyze the effect that the hypodermal layer would have on the laser, since it has been shown that fatty tissue has vastly different optical properties than that of the dermis and epidermis [50].

3.2.2.2 Experimental set-up and parameter

This experiment was performed in two parts, but in both cases, the laser fiber was fixed at 2 cm away from a vertically held piece of pig skin, simulating the fiber distance within the electrode, and the laser power was kept constant at 2.31 watts, which was a value determined to provide sufficient heating from previous pig skin calibration tests. The first portion of the experiment used a power meter at the back side of the pig skin to measure the amount of laser light transmitted through the sample over time (Figure 18). Data points were acquired every 5 seconds for a total laser exposure time of 3 minutes.

The next experiment replaced the power meter with a thermal camera, which was used to observe the changes in thermal distribution over prolonged laser exposure time at the rear of the

sample. This data trend would reveal how much heat would diffuse through the sample over time. Data points in this test were collected every 10 seconds for a total of five minutes, three minutes with the laser on and two minutes with the laser off to measure how the sample cools off.

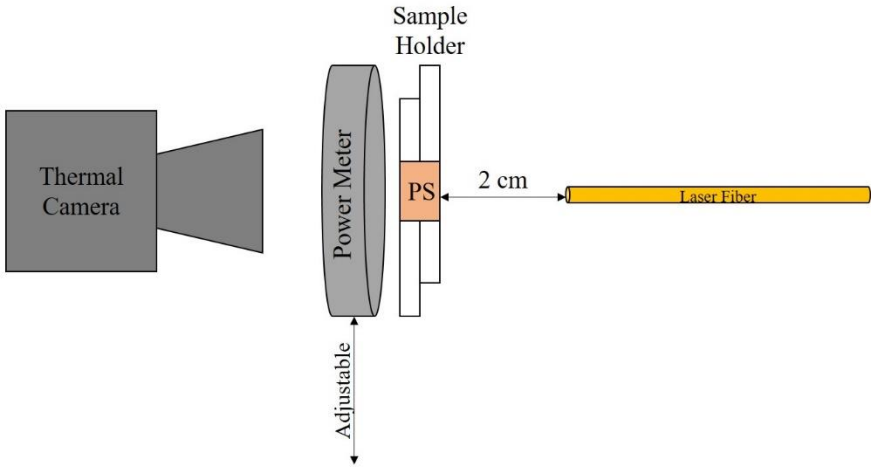

Figure 18: Pig skin absorption study set-up. The first part of the experiment used the power meter to measure the amount of power transmitted through the sample at intervals of 5 seconds for a total of 3 minutes (with the laser on). In the second part of the experiment, the power meter was removed and a thermal camera, placed 25 cm away from the sample, was used to measure the thermal distribution of the heating. The thermal camera acquired images every 10 seconds for a total of 5 minutes (3 minutes with the laser on and 2 minutes for a cool down).

3.2.2.3 Data collection and processing

Collected data was processed using Matlab, where the computation of the optical equations (Equations 6-10) as well as the curve fitting for the calculated data was performed. The collected

thermal images were processed in ImageJ, where the images were calibrated for correct dimensions and analyzed using 2D profile plots and 3D surface plots.

3.2.3. RESULTS AND DISCUSSION

Starting with the experimental results from the power meter test, there were significant changes observed in the optical properties of the pig skin sample from prolonged exposure to laser irradiation. Each tissue sample was able to retain the laser light for up to 30 seconds but once it passes this threshold, a consistent decrease in the absorption coefficient was observed (Figure 19). Despite this trend being observed for all samples, the extra fatty layer caused the absorption coefficient to be lower from the start. This is attributed to the hypodermal layer having a high scattering coefficient than the dermis or epidermis, causing less light to be absorbed [50-52]. These results are comparable with *in vivo* and *in vitro* optical studies performed on human skin [53, 54].

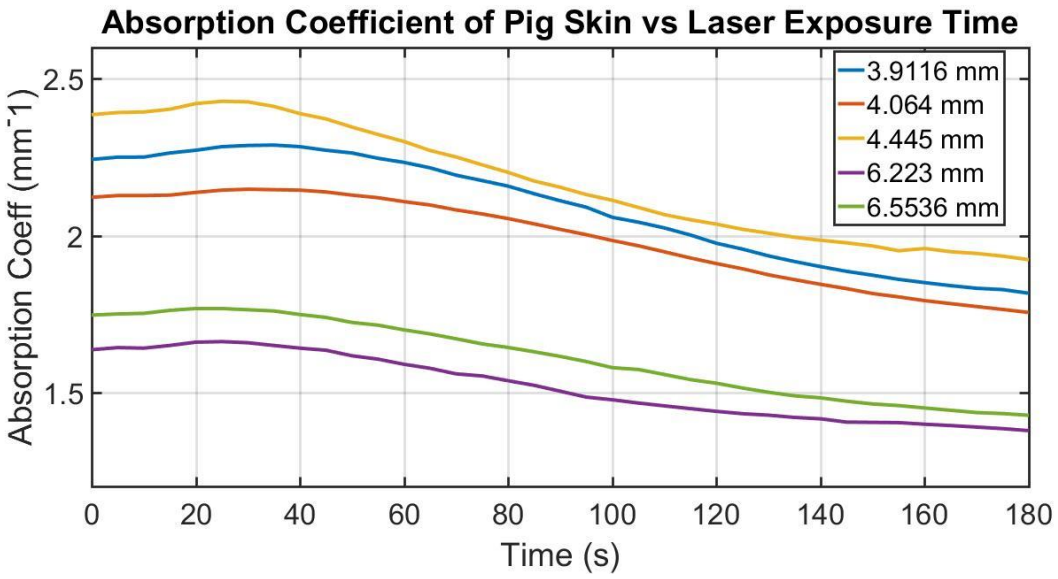

Figure 19: Absorption coefficient over laser exposure time. Analyzed using varying thickness of pig skin. Laser power was kept constant at 2.3W and was turned off at 180 seconds. Differences in sample thickness is attributed to increased layer of fatty tissue.

It was also observed that the laser is able the physically penetrate deeper into the skin over time (Figure 20). While this may seem like a relatively small change over 3 minutes, less than 0.1 mm^2, this shows that there is an increase in tissue penetration at longer exposure times, which can lead to deep heating of the tissue. It is very possible that a higher laser power setting could potentially increase the rate at which this penetration increases but this can cause unnecessary surface tissue damage. These results suggest that prolonged exposure to the laser irradiation lowers the absorption characteristics of the surface tissue and allows the laser light to penetrate deeper into the sample, resulting in deep tissue heat absorption.

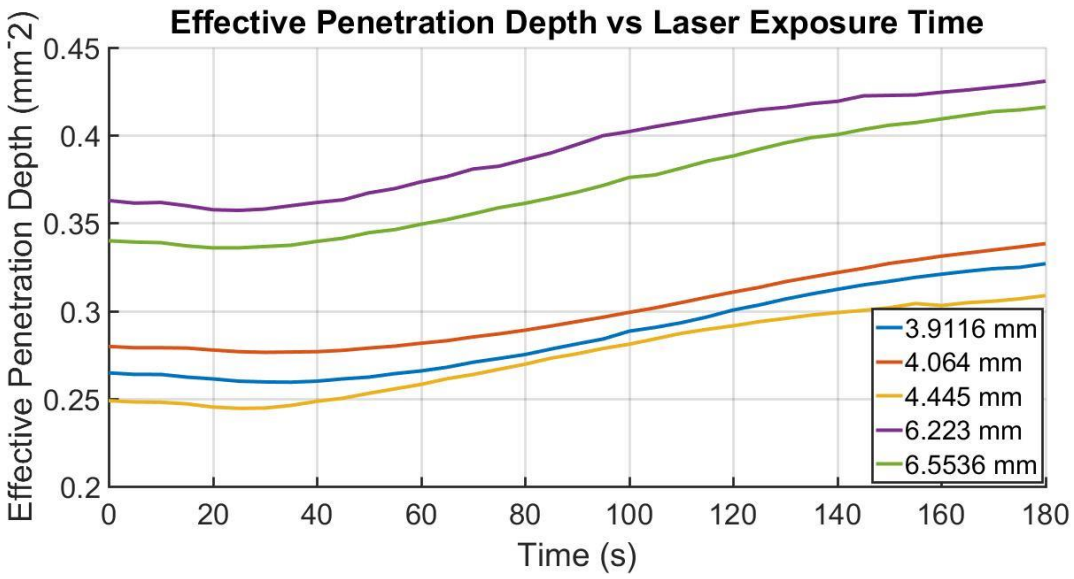

Figure 20: Effective penetration depth of the laser over laser exposure time. Analyzed using varying thickness of pig skin. Laser power was kept constant at 2.3W and was turned off at 180 seconds. Differences in sample thickness is attributed to increased layer of fatty tissue.

The heat distribution through the back of the skin followed a similar trend to that of the absorption coefficient. For the first 20-30 seconds of exposure, there is little to no heat increase observed at the back of the sample. However, after this delay, a large increase in temperature is observed over time. This suggests a correlation between these results and that of the absorption results, specifically in the overall trends. The longer the sample is exposed to the laser light, the more the absorption coefficient decreases, allowing more light to pass through. Increased intensity of light passing through the sample results in an increase of heating deep within the sample, as seen in the trend shown in Figure 21.

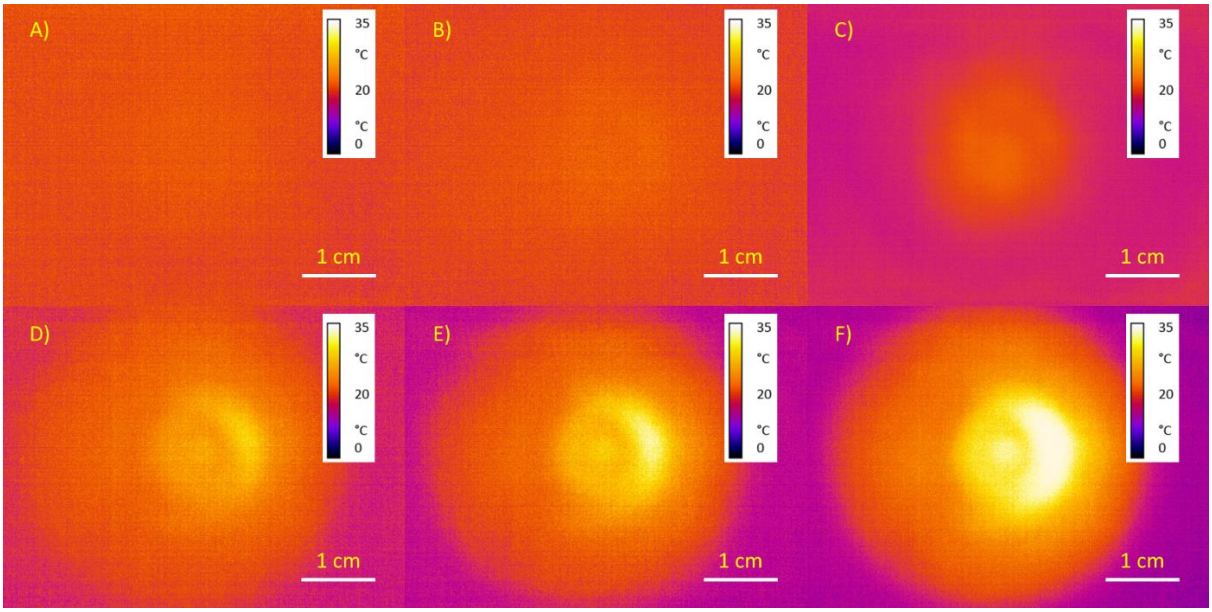

Figure 21: Thermal camera results and calibration images. Images are shown at laser exposure time = 0 (A), 30 (B), 60 (C), 90 (D), 120 (E), and 180 (F) seconds. The ring that begins to appear around the edge of the camera is the outline of the camera lens and appears due to the different of heat intensity observed by the lens and the ambient temperature around it.

Using ImageJ image processing software, the 2D images were translated into 3D surface plots in order to better visualize the heat distribution of the laser irradiation. An example of a generated surface plot is shown in Figure 22, where the image taken at 150 seconds laser exposure was used. As expected, the diffusion of the heat follows a gaussian profile, matching the profile of the laser beam determined by the knife edge technique. The area of the thermal distribution at the peak laser irradiation was found to be about 2 cm^2, which is less than the area between the needles of the electrode, 3.5 cm^2. However, this area only accounts for the peak temperature reading of 35℃. The entire heating area was determined to be ~4 cm^2, which is sufficient enough to cover the entire region between the needles. This large amount of heat

diffusion also suggests that the 6mm diameter spot size of the laser fiber is sufficient for penetration heating.

It is important to note that the diffusion of the heat was only measured through the rear of the sample. Based on heat diffusion dynamics, the area of heating on the surface of the skin is expected to be larger on the surface of the tissue [55]. This experiment primarily focused on the penetration aspect of the heat diffusion to ensure that the target would be heated internally rather than just on the surface.

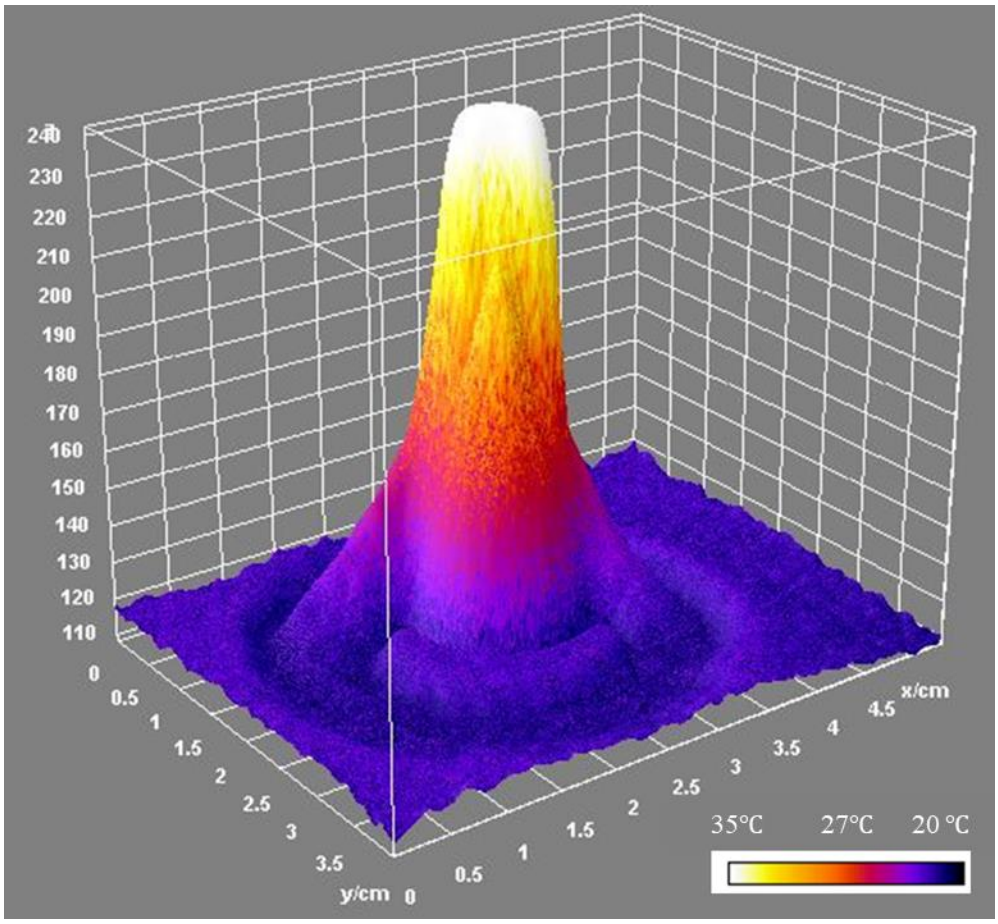

Figure 22: 3D surface plot of thermal camera image using ImageJ. Using the 2D image taken after 150 seconds of laser exposure, a 3D surface plot was implemented using the pixel intensity as the Z-axis. The value of 110 pixels corresponds to a temperature of 22℃ *while the peak value of 240 pixels corresponds to a value of 35*℃.

These results suggest that the penetration depth of the heat provided by the laser is directly related to the change in absorption characteristics. Prolonged exposure to the laser irradiation decreases the absorption characteristics of the sample, allowing the laser light to penetrate deeper into the sample, which in turn generates more heat diffusion. It has been shown that absorption characteristics of the dermal and epidermal layers of the skin provide a relatively constant decrease trend after 30 seconds of laser exposure. The addition of a larger hypodermal layer does

not alter this trend shape but shifts it to a lower starting value, due to its high scattering properties. Samples with larger hypodermal layers, i.e. more fat, will require a longer exposure to the laser for complete penetrative heating. It was also shown that the 2 cm distance from the laser fiber to the tissue surface was sufficient enough to facilitate adequate heat diffusion.

3.3. PROOF OF SYNERGY USING *IN VITRO* EXPERIMENT

The purpose of this study was to analyze the synergistic effect between moderate heating and pulsed electric fields as well as validate that this treatment would be effective in eliminating cancer cells. Before transitioning into animal experiments, it is important to validate the model. This not only saves time and resources but it also allows for a better treatment of the animals *in vivo* since the *in vitro* results will provide firm starting conditions for their treatment.

3.3.1. Methods and materials

3.3.1.1 Pan02 cell culture procedure

A murine pancreatic adenocarcinoma Pan02 cell line, incubated at 37℃ with 5% CO_2 and cultured using a 3D agarose cell-culture model was used for this *in vitro* study [56]. Each cell culture was prepared as follows [57]. The cells were incubated in a base layer of 900 μL 2.5% low-gelling temperature agarose gel, in complete media, and was applied to a 12 well tissue culture plate. This plate was then chilled to 4℃, at which the point the cells suspended and 3 x 10^6 Pan02 cells, which were resuspended in 1 mL of 1% low-gelling agarose gel, was laid over the base layer. At this point, the culture was returned to 4℃ for four minutes after which the cell cultures were incubated at 37℃ for 20 minutes.

3.3.1.2 Pulse generator

A ECM 830 Square Wave Electroporation System was used for all applications of PEF in this thesis. The pulser had a maximum voltage output of 3 kV, a variable pulse width from 10 μs to 10 secs and a variable pulse repetition rate. The electric pulses are transmitted to the electrode though banana plug connections and high voltage wires rated for 25 kVDC. For every experiment, the voltage waveforms were monitored using a Tecktronics ® Model P0015A voltage attenuator and recorded on a LeCroy Waverunner 64xi Oscilloscope.

3.3.1.3 Experimental set-up and parameters

The PEF were applied using a 2-needle electrode inserted directly into the cell culture with pulsing conditions of a 100 μs pulse width, a frequency of 1 Hz, 80 pulses and electric field strengths of 0, 0.750 and 1.5 kV/cm with and without heating. A heat block was used to raise the temperature of the entire cell culture to 43℃ and was maintained for at least one minute before applying the electric pulses. The purpose of using the heat block rather than the laser at this point was to provide an optimal heating condition, which would give more ideal results. Temperature was monitored using a combination of a thermometer attached to the heat block and a thermocouple inserted into the edge of the cell culture. Each condition was performed in triplicate for statistical significance.

3.3.1.4 Imaging procedure

Immediately after treatment, 1 mL of fresh media was added to each treated culture and were incubated at 37℃ with 5% CO_2 for 90 minutes. After this incubation period, Propidium Iodide (PI, 4 µg/ml) was added to the media, which was then returned to the incubator for another 30 minutes. Once this staining period was complete, images of the ablation zone were obtained using a fluorescence stereomicroscope, with each image being collected under identical exposure parameters. All images were processed using ImageJ and are reported as integrated fluorescence density in relative fluorescence units (RFUs).

3.3.2. RESULTS AND DISCUSSION

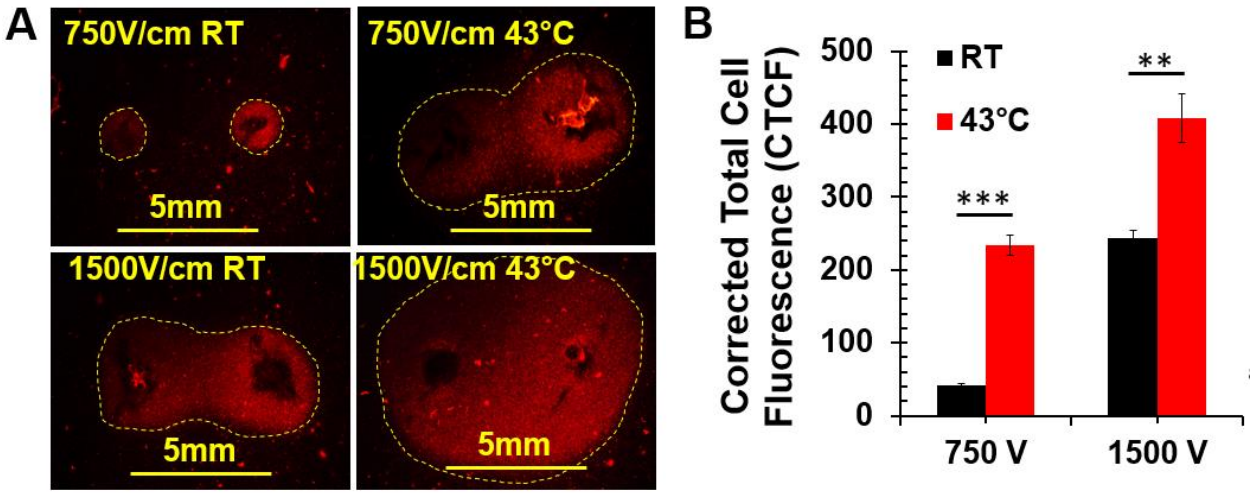

*Figure 23: In vitro synergy results using a 2-needle electrode and a heat block. A) 2-needle electrode treatments at varying electric field strengths and with/without heating. B) Corrected Total Cell Fluorescence comparison between the voltage and heating conditions. Treatments per group =3-4. ** p<0.01 and ***p<0.001 for pulsing only vs pulsing +heat by t-test.*

When applying heating of 43℃ by itself for two minutes, there was no cell death observed, showing that the heating alone is not enough to induce cell death. Applying 750 V/cm without the heating protocol resulted in cell death to only occur around the needles, where the electric field would be the strongest (Figure 23). Once a uniform heating of 43℃ was added, there was a significant increase in cell death, a factor of 5.67 more than the pulsing alone, showing that the elevated temperature was compensating for the areas of weaker field strength. What is even more interesting is that the addition of heat to 750 V/cm produced similar results to that of a field double in strength by itself, 1.5 kV/cm. This means that not only does heating help increase the effective treatment area of the PEF, but it is also able to reduce the required electric field intensity to achieve uniform cell death at the treatment site. Even adding the heating protocol to the higher voltage condition results in larger areas of cell death, like in the case of 1.5 kV/cm where the addition of heat provided a 1.67-fold increase of cell death when heat was added.

These results show that there is a significant synergistic effect between moderate heating and PEF. The greatest effect is seen at the lower applied electric fields, where the combination of these treatments resulted in cell death similar to that of an applied voltage twice as large. Results suggest that the combination of PEF and moderate heating should allow for greater tumor size reduction, or even elimination, at lower applied electric fields.

Chapter 4

THERMALLY ASSISTED PEF TREATMENT OF PANCREATIC CANCER

This controlled heating system has been used in the treatment of various biological experiments, such as enhancement of gene electrotransfer, nanosecond PEF treatment of lung squamous tumors in mice, and microsecond PEF treatment of pancreatic cancer in mice. The experiment involving the pancreatic tumor treatment will be presented in this chapter. In addition to the *in vivo* mouse experiment, an *in vitro* study was performed using 3D agarose cultures to demonstrate the effects that the 4-needle electrode and laser surface heating would have on cells. These results have been published in Scientific Reports in September 2017 [57].

4.1. PAN02 *IN VITRO* TREATMENT USING CONTROLLED HEATING SYSTEM

This *in vitro* experiment is using the same procedure as the one described in section 3.3, the only difference being that the 4-needle electrode and laser were used to apply the electric fields and heat the culture respectively. The laser heating protocol used for this system as well as the comparison between this treatment to that of the heat block (section 3.3) will be discussed. Please refer to section 2.1 and 4.2 for the specifications of the laser and pulser used in this study.

4.1.1. Materials and methods

4.1.1.1 Heating protocol

To ensure that there was sufficient heat penetration during the treatment, a standard heating protocol had to be determined. An initial protocol was created using the results from the absorption study, which stated that the laser irradiation would start to penetrate through the sample after 30 seconds of laser exposure time. This protocol was tested on mice carrying an induced Pan02 tumor, using a 40-100 mm^3 diameter tumor sizes, which were used as calibration for the in vivo experiment discussed in section 4.2. A thin thermocouple was inserted into the base of the tumor and the laser heating was applied to the surface of the tumor at a temperature setting of 43℃. Results from this calibration showed that it took an average of 30-60 seconds for the thermocouple to reach 42℃ so it was determined that a pre-heat treatment of one minute should be applied to ensure the entire tumor is heated. This protocol, shown in Figure 24, was used for all remaining experiments in this chapter.

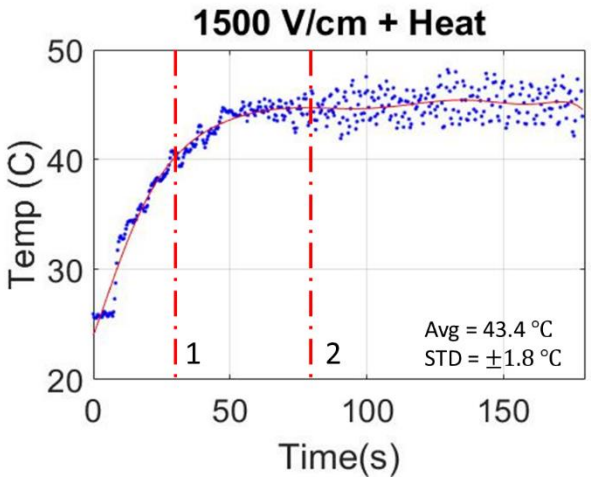

Figure 24: Standard heating protocol. When the laser is first turned on, the time it takes to reach 40℃ is monitored. Once this threshold is passed, a one minute timer for pre-heating of the target is started. After this timer expires, the application of PEF can begin.

4.1.1.2 Experimental set-up and parameters

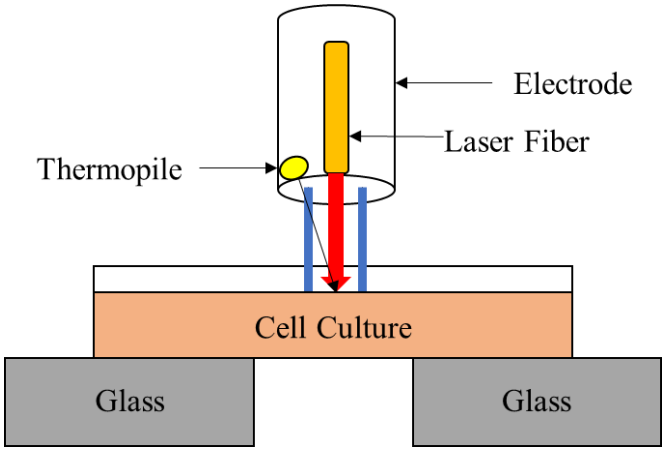

Figure 25: In vitro experimental set-up using electrode and laser control device. The exposed portions of the needles were inserted into the 3D agarose gel Pan02 tumor model and was treated with PEF and moderate surface heating provided by the laser.

The 4-needle electrode was inserted directly into the center of the culture, fully covering the exposed portion of the needles (Figure 25). The controlled infrared heating system was used to heat the culture up to 43℃ using the previously described heating protocol and cell culture temperature was monitored by as external thermocouple that was inserted at the edge of the well. The pulsing parameters were similar to the previous *in vitro* experiment using the 2-needle electrode and heat block, using an electric field strength 0 and 750 V/cm with and without heat, a pulse width of 100 µs, a repetition rate of 1 Hz and 80 total pulses. The fluorescence images were processed in the same way as the previous *in vitro* experiment. Refer to section 4.2 for the imaging procedure.

4.1.2. Results and discussion

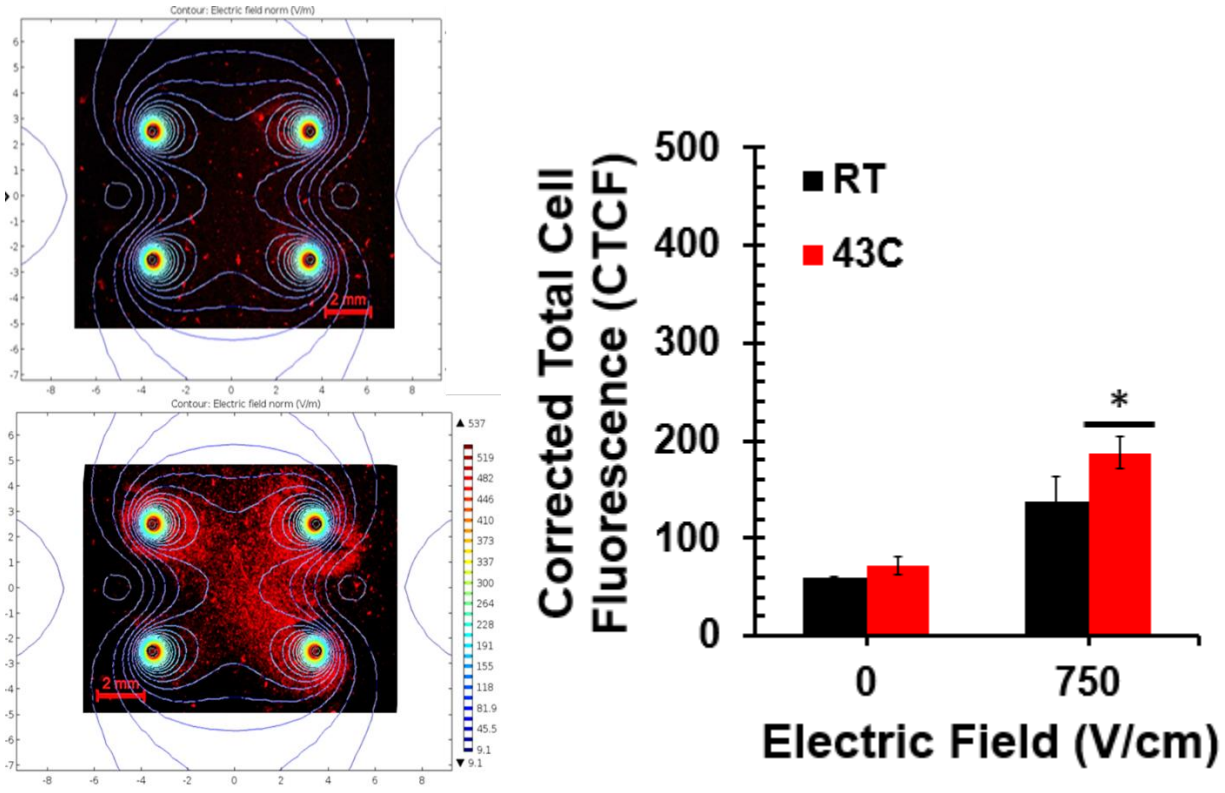

*Figure 26: 4-needle electrode with laser heating in vitro results. Top left: 750 V/cm only; Bottom left: 750 V/cm + heating protocol. Right: Comparison of Corrected Total Fluorescence (CTCF) of IRE conditions and IRE + heating conditions. * $p < 0.05$ by t-test*

Comparing laser heating alone and the control group, there was no significant difference between them, confirming the results previously shown that the heating alone is not enough to cause cell death. Like in the other *in vitro* study, applying 750 V/cm without the heating protocol resulted in cell death to only occur around the needles, where the electric field would be the strongest (Figure 26). When applying the laser heating protocol, there was a significant increase in cell death, a factor of 1.4 more than the pulsing alone, showing that the elevated temperature was compensating for the areas of weaker field strength. This increase in cell death is much

lower than the increased shown using the heat block, since the only the center of the culture is being heated in this case. Despite this, there is still a significant increase in treatment area when combining the moderate surface heating and the PEF treatment, once again suggesting that these protocols are complementing each other.

4.2. PAN02 *IN VIVO* TREATMENT USING CONTROLLED HEATING SYSTEM

The purpose of this study is to investigate the effect that controlled surface heating will have on tumors when combined with PEF. This was among the first studies to use controlled laser heating during the application of PEF. Proving that this device is effective would allow it to branch out into other biological tests, such as treatment of other cancer strains. In addition to monitoring the heating, the impedance of the tumor was monitored per pulse through a custom voltage-current monitor, or VI box. Observing the physical changes in the tumor during treatment can help shed light on how the PEF are effecting the tumor and if the laser heating is significantly impacting them.

4.2.1. Materials and methods

This *in vivo* procedure uses the same cell line, pulse generator and heating protocol previously described. The preparation and guidelines for the mice and the specific experimental parameters will be discussed in this section. Refer to section 2.1 and 3.3 for the specifications of the laser and pulser used in this experiment.

4.2.1.1 Mouse and tumor model

Female black mice, C57BL/6 mice, of 6–8 weeks of age were injected with 1×10^6 Pan02 cells in 50 μL Dulbecco's phosphate buffered saline (DPBS) on the left flank. See section 4.2 for Pan02 cell line description. The size of primary tumor was measured twice weekly with digital calipers. Tumor volume was determined using the following formula:

$$V = \frac{\pi a b^2}{6} \tag{11}$$

where (a) is the longest diameter and (b) is the shortest diameter perpendicular to (a) [58]. Mice were euthanized at the end of the follow-up period or when they met criterion described at experimental endpoints, such as large tumor volumes or declining health of the mice. All experimental protocols were approved by Old Dominion University Institutional Biosafety Committee (IBC) and Institutional Animal Care and Use Committee (IACUC). And all experiments were performed in accordance with relevant guidelines and regulations.

4.2.1.2 Voltage and current monitor system

Observation of the change in tumor impedance was performed by a Voltage Current Monitor Box, or a VI Box. This VI box (Figure 27) utilized two voltage attenuator probes, with an attenuation ratio of 1000:1, and a current viewing resistor, that used the voltage drop on the resistor to determine the pulse current applied to the tumor, to monitor the change in tumor impedance in real time using Equations 11 and 12:

$$A = \frac{V1 - V2}{R_{cu}} \tag{12}$$

$$R = \frac{V2}{A} \tag{13}$$

Where *A* is the current, *V1* is the voltage supplied by the BTX 830 pulse generator, *V2* is the voltage deliver to the electrode, R_{cu} is the current view resistor and *R* is the impedance of the tumor.

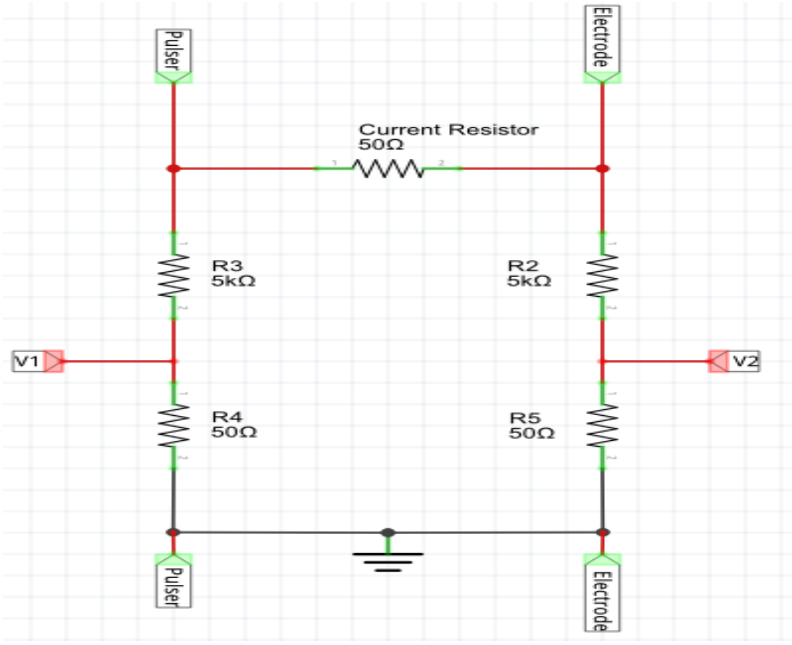

Figure 27: VI Box Diagram. Voltage readings V1 and V2 were measured directly with the oscilloscope. The current and impedance values were calculated based on these two values. Circuit isolated from electrical noise using metal enclosure.

The voltage signals *V1* and V2 were measured and stored using the LeCroy 64xi oscilloscope while the current and impedance values were calculated after the treatment was completed. Like the control system, this box was isolated within a metal casing to prevent electrical interference. It is important to note that since the voltage of pulse was used to determine the impedance of the tumor, it is not possible to measure the impedance before or after pulsing using this device.

4.2.1.3 Experimental set-up and parameters

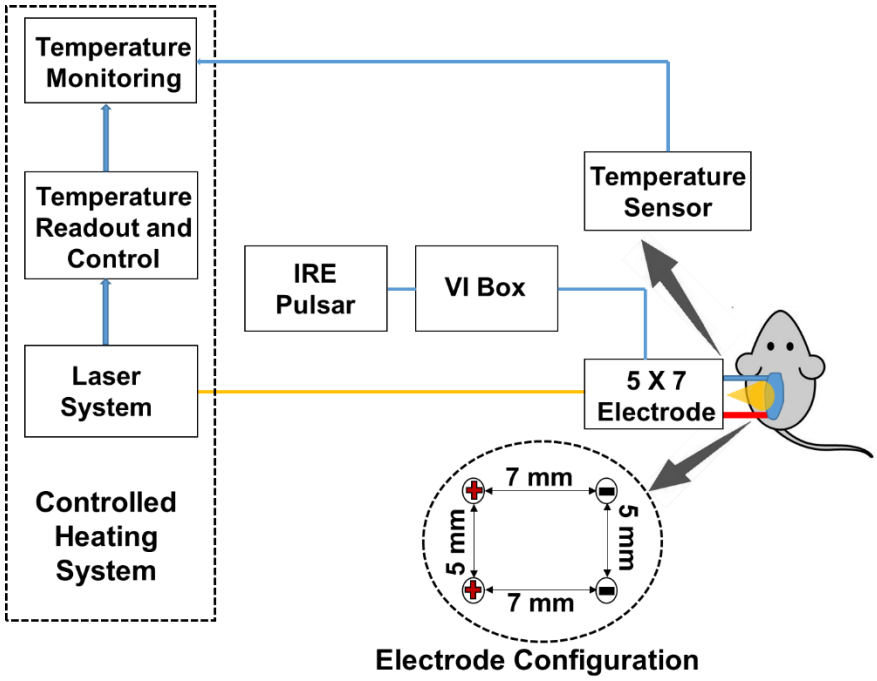

Figure 28: Experimental set-up for in vivo pancreatic tumor tests. The controlled infrared system a laser power supply, a 4-needle electrode with an integrated 980-nm laser optic fiber and thermopile to control the surface heating, and a laptop with temperature monitoring and laser control software. Electric pulses are generated by a BTX ECM 830 Square Wave Electroporation System (IRE Pulsar) and the voltage/current waveforms were monitored using a VI box and a LeCroy 64xi Waverunner Oscilloscope.

The Pan02 tumors ranging from 200-400 mm^3 in size, determined by Equation (10), were treated with either IRE or IRE + moderate surface heating (MHIRE) with parameters: 100μs pulse width, 1 pulse per second, 90 pulses and voltage intensities of 0, 750 V/cm, 1500 V/cm, 2000 V/cm and 2500 V/cm. Once the treatment was complete, the mice were monitored daily and the tumors were remeasured every 3-4 days.

4.2.1.4 Data collection and processing

Temperature trends and laser timings from the heating treatment were collected using the GUI and processed using Matlab, where the temperature trend fits were created using the curve fitting toolbox. The voltage waveforms *V1* and *V2* were collected using the LeCroy 64xi's save function and processed in Matlab, where computation of the current and impedance trends per pulse were performed.

4.2.2. Results and discussion

4.2.2.1 Laser Heating Trends

An average surface temperature of 44–45 °C was achieved with a fluctuation within 42 °C to 47 °C. The rise time to reach 45 °C was varied for each tumor because of the difference in tumor shape and whether there was a center necrosis or ulcerations. Noticeably, a much longer pre-heating time was needed for MHIRE with 2 kV/cm or 2.5 kV/cm (Figure 29). These high voltage conditions had a high occurrence of surface electrical breakdown so ultrasound gel was applied on the tumor surface and around the insertion sites of the needles to help prevent this potential

electrical breakdown. The ultrasound gel caused the surface temperature to decrease and the heating time to increase, since the laser had to heat the gel before heating the tumor itself.

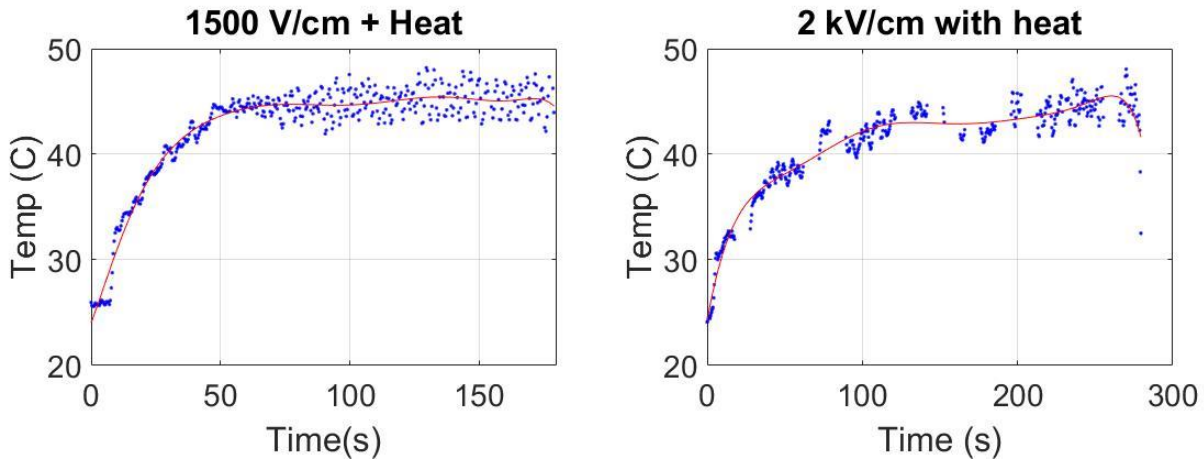

Figure 29: In vivo temperature trends at different electric field intensities. The longer heat up times seen at 2 kV/cm is attributed to the ultrasonic gel applied to the needles to prevent local electrical breakdown. Each trend achieved an average temperature of 43℃ with a standard deviation of ±2℃.

The temperature trend of the pulsing only conditions were also monitored, to see if there is a significant joule heating effect from the higher voltage conditions (Figure 30). There was a noticeable temperature increase of the tumor due to the pulsing conditions alone was observed. Maximal temperature increase of the tumor was 7.5 °C for IRE with 2.5 kV/cm and 4.7 °C for IRE with 2 kV/cm. Because of the relative low base temperature of the tumor, which was between 23 °C to 27 °C, especially when the dielectric gel was applied, the temperature increase due to IRE is likely not to impact the tumor ablation.

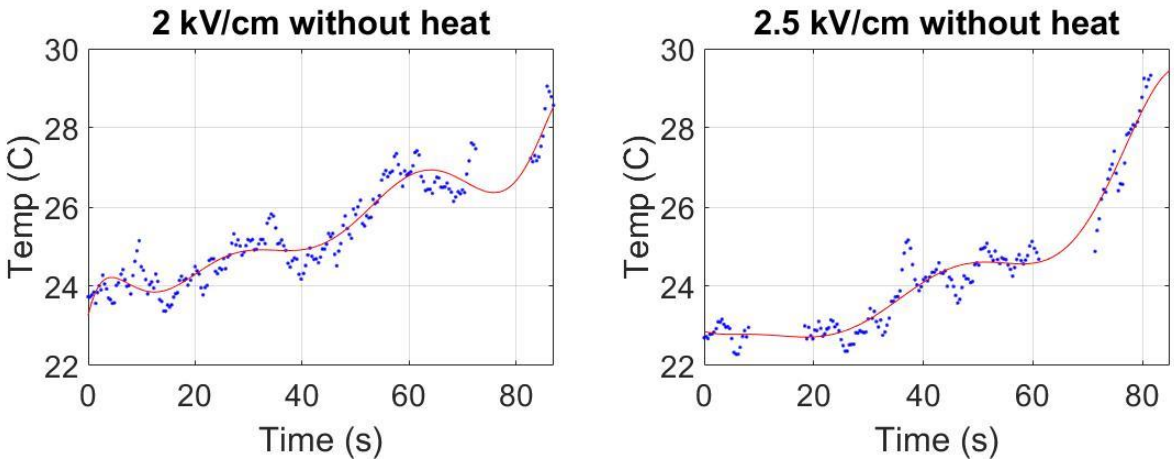

Figure 30: Joule heating measurements. Heat generated by the PEF only was monitored using the thermopile. Results show a minor increase in heat over time.

4.2.2.2 Impedance Measurements

From the impedance curves (Figure 31), the baseline impedance of each tumor varied but the addition of moderate heat reduced the starting value by 200–300 Ω or 15–38% of the baseline impedance, 750 to 1100 Ω. The reduction of the impedance over the pulse train can be correlated to strength of the applied electric fields, the higher electric field, the more the impedance was reduced by the end of the treatment. The electric field strength was kept constant for each pulse so the change in impedance over each pulse can be attributed to an increase of current. The average drop of impedance was 39.1 to 46.6% for MHIRE with 2000 to 2500 V/cm and 22.4 to 30.5% for IRE with the same electric field. Additionally, it appears that moderate heating also reduces the fluctuation of impedance changes, which may indicate that moderate heating enhances uniformity of the tumor dielectric property. A clinical trial treating pancreatic cancer in humans using microsecond PEF also suggests a correlation between the decrease in tumor

impedance and tumor regression/elimination [59], suggesting that the tumor impedance plays a significant role in the elimination of tumors.

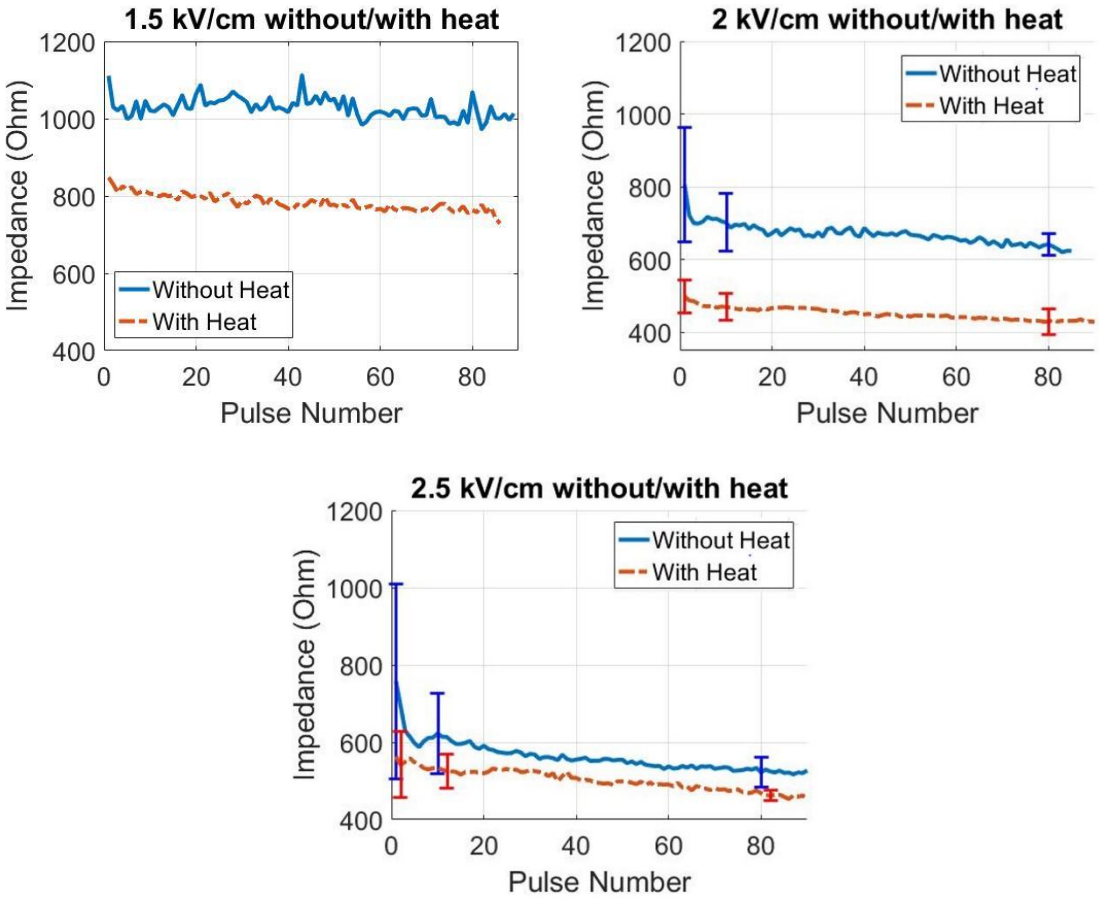

Figure 31: Impedance Trends at different electric field intensities. Impedance values were measured at the delivery of each pulse. Without heat and with heat sample size = 7-8. Error bars shown at pulse 1, 10 and 80.

4.2.2.3 Tumor Regression and Elimination

IRE treatments using 750 and 1500 V/cm without heat had little impact on the tumor growth. However, a synergistic effect was seen in the IRE treatment when the tumor was preheated using the heating protocol for both 750 V/cm and 1500 V/cm treatments (Figure 32). A significant decrease of tumor size was seen in animals treated with MHIRE at 750 V/cm only at one-time point at post-treatment day 8, whereas tumors treated with MHIRE at 1500 V/cm were all significantly smaller than control group or the IRE alone group at all time points on post-treatment days 4, 7, 11, 13 and 14. Despite this reduction in tumor growth, there was no complete tumor regression observed under these two IRE protocols, even with the addition of heat.

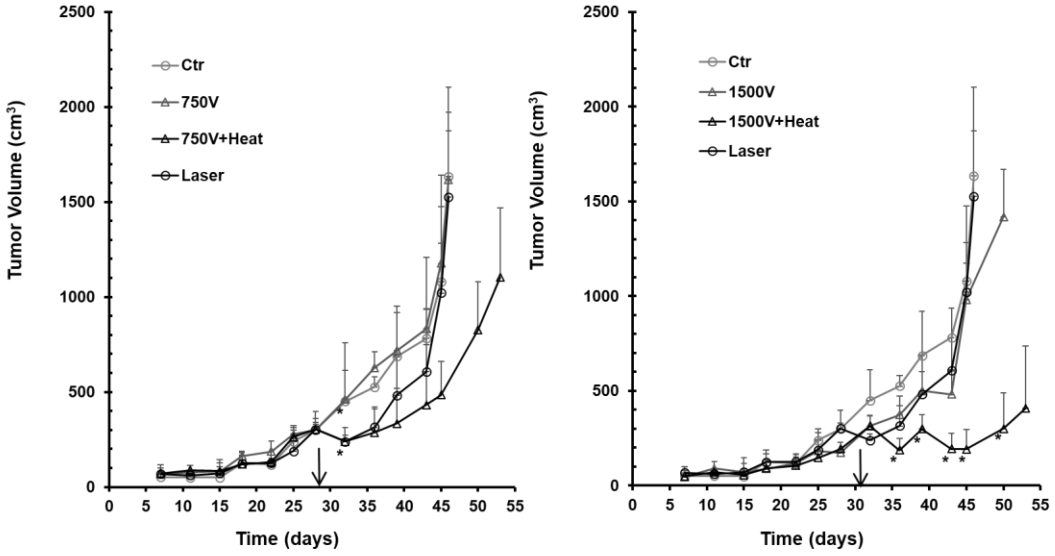

*Figure 32: 0.75-1.5 kV/cm tumor growth curves for in vivo treatment. Treatments occurred on day 28 or 31 indicated by black arrow. Ctr: no treatment (n = 4 mice per treatment group); Laser: tumor heated with laser using the heating protocol; 750 V, 1500 V: IRE at 750 V/cm or 1500 V/cm (n = 4 mice per treatment group); 750 V + Heat or 1500 V + Heat: tumor preheated using heating protocol with IRE at 750 V/cm (n = 7 mice per treatment group) or 1500 V/cm (n = 8 mice per treatment group). Right: *p < 0.05; Left: *p < 0.01 or p < 0.001 for MHIRE vs IRE or Ctr by One Way ANOVA.*

The Kaplan-Meier survival curves are shown in Figure 33. Despite the higher electric fields of 2-2.5 kV/cm, IRE treatment alone could not achieve tumor free animals. It only extended the medial survival for 3 days with 46 days median survival compared to 43 days median survival for the control tumor animals. However, the addition of moderate surface heating significantly extended median survival by almost two times with 84 days compared to control mice. More importantly, 56% of the tumor-bearing mice that were treated with MHIRE were tumor-free. No severely sick animals were found for IRE or MHIRE treatment at 750–1500 V/cm, however, at high electric field 2000–2500 V/cm 5/13 mice in IRE group and 2/11 mice in IRE + heating

group were euthanized due to severe dehydration, high pain scores or severe sickness. The causes of serious adverse events were likely related to large tumor necrosis or intestine/adjacent tissue necrosis.

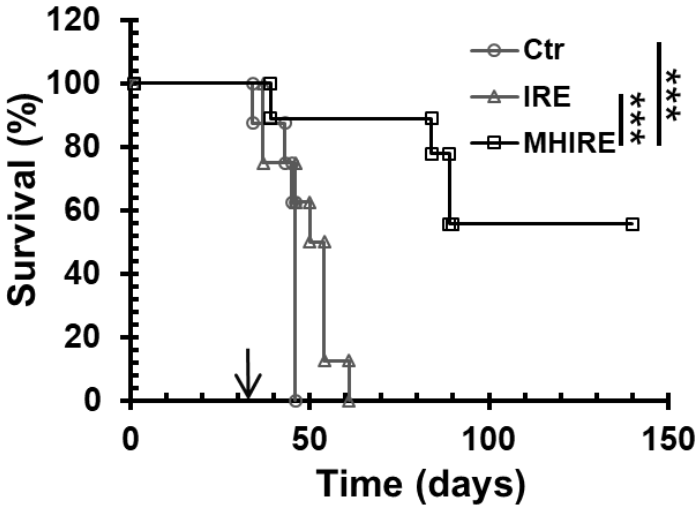

*Figure 33: 2-2.5 kV/cm survival curves for in vivo treatment. Treated on day 31 indicated by arrow. Ctr: no treatment (n = 8 mice per treatment group); IRE: treated with IRE (n = 8 mice per treatment group); MHIRE: tumor preheated using heating protocol with IRE (n = 9 mice per treatment group). ***p < 0.001 for MHIRE vs IRE or Ctr by LogRank test.*

This study sought to increase the efficiency of the current IRE treatment protocol of pancreatic cancer by moderately heating the tumor before and during the treatment. It has been shown that there are synergistic effects between moderate surface heating and IRE in both *in vitro* cancer cell ablation and *in vivo* tumor reduction. Moderate surface heating is able to significantly enlarge tumor ablation zone *in vitro* (Figure 26) and reduce tumor growth *in vivo* (Figure 31). It is also able to produce results similar to that of higher electric field strengths,

allowing for regression at safer pulsing conditions. Laser heating was also shown to have a significant impact on the impedance of the tumor, reducing it by 15–38% before the PEF treatment began. Because complete tumor ablation only occurred with MHIRE group, this indicates that a large reduction of impedance maybe necessary for complete tumor ablation.

Chapter 5

SUMMARY AND FUTURE WORK

Pulsed electric fields have many applications in the medical research field, including cancer treatment, gene therapy and surface sterilization. However, the devices used to deliver these PEFs often leave much to be desired. Many of these devices, especially in the case of needle or pin electrodes, require much higher electric fields in order to see the desired result. This can lead to unnecessary electrical breakdown during treatment and even toxic effects from higher electric fields. Based on the results from the in vitro experiments, the application of moderate surface heating can be used to alleviate the requirement for high intensity electric fields by compensating for the areas with weaker strength fields.

In summary, an infrared controlled heating device was created to investigate the synergistic effect between moderate surface heating provided by a 980nm laser and pulsed electric fields. Initially, integration of a surface temperature sensor into a PEF electrode proved to be challenging due to its physical restrictions and interference from electrical noise. However, by applying data correction techniques and isolating the small voltage electronics, it is possible to reliably monitor the surface irradiation in real time using this set-up.

The heating effects caused by this system, including changes in tissue properties and the diffusion of the laser irradiation into the tissue, were also characterized. Results from various *in vitro* and *in vivo* experiments suggests that the addition of this heating device to the PEF treatment can result in a larger treatment area and lower the electric field intensity required to see tumor regression.

Further testing is required to solidify this conclusion and further studies should focus on optimizing the communication between the components in the system as well as optimize the laser power distribution to create of more uniform and penetrative heating.

REFERENCES

1. James C. Weaver, Y.A.C., *Theory of electroporation: A review.* Bioelectrochemistry and Bioenergetics, 1996. **41**: p. 135-160.
2. Semenov, I., et al., *Recruitment of the intracellular Ca2+ by ultrashort electric stimuli: the impact of pulse duration.* Cell Calcium, 2013. **54**(3): p. 145-50.
3. Beebe, S.J., N.M. Sain, and W. Ren, *Induction of Cell Death Mechanisms and Apoptosis by Nanosecond Pulsed Electric Fields (nsPEFs).* Cells, 2013. **2**(1): p. 136-62.
4. Beebe, S.J., et al., *Transient features in nanosecond pulsed electric fields differentially modulate mitochondria and viability.* PLoS One, 2012. **7**(12): p. e51349.
5. Shan Wu, Y.W., Jinsong Guo, Qunzhi Chen, Jue Zhang, Jing Fang, *Nanosecond pulsed electric fields as a novel drug free therapy for breast cancer: an in vivo study.* Cancer Lett, 2014. **343**(2): p. 268-74.
6. Indran, I.R., et al., *Recent advances in apoptosis, mitochondria and drug resistance in cancer cells.* Biochim Biophys Acta, 2011. **1807**(6): p. 735-45.
7. Morotomi-Yano, K., et al., *Activation of the JNK pathway by nanosecond pulsed electric fields.* Biochem Biophys Res Commun, 2011. **408**(3): p. 471-6.
8. Scott W.Lowe, A.W.L., *Apoptosis in cancer.* Carcinogenesis, 2000. **21**(3): p. 485–495.
9. S.J. Beebe, P.M.F., L.J. Rec, *Nanosecond, high-intensity pulsed electric fields induce apoptosis in human cells.* FASEB J, 2003. **17** (1493).
10. Wei Ren, S.J.B., *An apoptosis targeted stimulus with nanosecond pulsed electric fields (nsPEFs) in E4 squamous cell carcinoma.* Apoptosis, 2011. **16**(4): p. 382-93.

11. Staples, G. *Using the Arduino Uno's built-in 10-bit to 16+-bit ADC (Analog to Digital Converter)*. 2015; Available from: http://www.electricrcaircraftguy.com/2014/05/using-arduino-unos-built-in-16-bit-adc.html.

12. *Electroporation-Based Therapies for Cancer: From Basics to Clinical Applications*. 2014: WoodHead Publishing.

13. Maruyama, H., et al., *Skin-targeted gene transfer using in vivo electroporation.* Gene Ther, 2001. **8**(23): p. 1808-12.

14. Rombouts, S.J., et al., *Irreversible Electroporation of the Pancreas Using Parallel Plate Electrodes in a Porcine Model: A Feasibility Study.* PLoS One, 2017. **12**(1): p. e0169396.

15. Adeyanju, O.O., H.M. Al-Angari, and A.V. Sahakian, *The optimization of needle electrode number and placement for irreversible electroporation of hepatocellular carcinoma.* Radiol Oncol, 2012. **46**(2): p. 126-35.

16. Yin, S., et al., *Nanosecond pulsed electric field (nsPEF) treatment for hepatocellular carcinoma: a novel locoregional ablation decreasing lung metastasis.* Cancer Lett, 2014. **346**(2): p. 285-91.

17. Cen, C. and X. Chen, *The Electrode Modality Development in Pulsed Electric Field Treatment Facilitates Biocellular Mechanism Study and Improves Cancer Ablation Efficacy.* Journal of Healthcare Engineering, 2017. **2017**: p. 1-10.

18. Bettaieb, A., P. K, and D. A, *Hyperthermia: Cancer Treatment and Beyond.* 2013.

19. Kaur, P., et al., *Combined hyperthermia and radiotherapy for the treatment of cancer.* Cancers (Basel), 2011. **3**(4): p. 3799-823.

20. J., v.d.Z., *Heating the patient: a promising approach?* Ann Oncol, 2002. **13**(8): p. 1173-84.

21. Lindquist, S., *The Heat-Shock Response.* Annual Review of Biochemistry, 1986. **55**(1): p. 1151-1191.

22. E. SOUIL, A.C., S. MORDON, A.T. DINH-XUAN, B.S. POLLA, M.BACHELET, *Treatment with 815-nm diode laser induces long lasting expression of 72-kDA heat shock protein in normal rat skin.* British Journal of Dermatology, 2001. **144**: p. 260-266.

23. Wust, B.H.a.P., *The biologic rationale of hyperthermia.* Cancer Treat Res, 2007(134): p. 171-184.

24. Bert Hildebrandt , P.W., Olaf Ahlers,Thoralf Kerner, Roland Felix , Annette Dieing, Hanno Riess, Geetha Sreenivasa *The cellular and molecular basis of hyperthermia.* Critical Reviews in Oncology/Hematology, 2002. **43**: p. 33-56.

25. Alfaifi, B., et al., *Computer simulation analyses to improve radio frequency (RF) heating uniformity in dried fruits for insect control.* Innovative Food Science & Emerging Technologies, 2016. **37**: p. 125-137.

26. Huang, Z., F. Marra, and S. Wang, *A novel strategy for improving radio frequency heating uniformity of dry food products using computational modeling.* Innovative Food Science & Emerging Technologies, 2016. **34**: p. 100-111.

27. Combes, N., et al., *Ablation of supraventricular arrhythmias in adult congenital heart disease: A contemporary review.* Arch Cardiovasc Dis, 2017. **110**(5): p. 334-345.

28. Multiphysics, C. *The Joule Heating Effect.* 2017; Available from: https://www.comsol.com/multiphysics/the-joule-heating-effect.

29. Hradecky, J., et al., *Ohmic heating: A promising technology to reduce furan formation in sterilized vegetable and vegetable/meat baby foods.* Innovative Food Science & Emerging Technologies, 2017. **43**: p. 1-6.

30. Hudson, D.E., et al., *Penetration of laser light at 808 and 980 nm in bovine tissue samples.* Photomed Laser Surg, 2013. **31**(4): p. 163-8.

31. Fodor, L., Y. Ullmann, and M. Elman, *Light Tissue Interactions.* 2011: p. 11-20.

32. Amy Donate, A.B., Chelsea Edelblute, Derrick Jung, Mohammad A. Malik, Siqi Guo, Niculina Burcus, Karl Schoenbach, Richard Heller, *Thermal Assisted In Vivo Gene Electrotransfer.* Current Gene Therapy, 2016. **16**(2): p. 83-89.

33. Thermometrics, *ZTP-135 Datasheet*, A.A. Sensors, Editor. 2014, Amphenol Advanced Sensors.

34. RAMLI, D.F.B., *THERMO MIRROR TO DETECT HUMAN BODY TEMPERATURE*, in *Engineering*. 1989, UNIVERSITI TEKNOLOGI MALAYSIA: UNIVERSITI TEKNOLOGI MALAYSIA. p. 71.

35. Schilz, J., *THERMOELECTRIC INFRARED SENSORS (THERMOPILES) FOR REMOTE TEMPERATURE MEASUREMENTS; PYROMETRY.* PerkinElmer Optoelectronics, 2011.

36. Koon Seok Lee, J.H.L., *Temperature sensing circuit using thermopile sensor*, L.E. Inc., Editor. 2001.

37. Labs, S., *AN118: Improving ADC Resolution by Oversampling and Averaging*, S. Labs, Editor. 2013. p. 1-22.

38. Coorporation, A., *AVR121: Enhancing ADC resolution by oversampling*, A. Coorporation, Editor. 2005, Atmel Corporation.

39. Zhou, Y., *An oversampling system for ECG acquisition.* Journal of Biomedical Science and Engineering, 2009. **02**(07): p. 521-525.

40. J. Magnes, D.O., J. Hartke, M. Fountain, L. Florence, V. Davis, *Quantitative and Qualitative Study of Gaussian Beam Visualization Techniques.* Cornell University Library, 2008: p. 5.

41. Chapple, P.B., *Beam waist and M^2 Measurement using a finite slit.* Optical Engineering, 1994. **33**(7).

42. Shayler, P.J., *Laser beam disribution in the focal region.* Applied Optics, 1978. **12**: p. 2673-2674.

43. de Araújo, M.A., et al., *Measurement of Gaussian laser beam radius using the knife-edge technique: improvement on data analysis.* Applied Optics, 2009. **48**(2): p. 393.

44. *The measurement of a transverse profile of laser beam by Knife Edge method*. 2013.

45. Christian Rossmann, D.H., *Review of temperature dependence of thermal properties, dielectric properties, and perfusion of biological tissues at hyperthermic and ablation temperatures.* Critical Review Biomedical Engineering 2014. **42**(6): p. 467-492.

46. Anderson, R.R. and J.A. Parrish, *The Optics of Human Skin.* Journal of Investigative Dermatology, 1981. **77**(1): p. 13-19.

47. Lister, T., P.A. Wright, and P.H. Chappell, *Optical properties of human skin.* J Biomed Opt, 2012. **17**(9): p. 90901-1.

48. Sarkar, S., et al., *Optical properties of breast tumor phantoms containing carbon nanotubes and nanohorns.* J Biomed Opt, 2011. **16**(5): p. 051304.

49. A. Bhandari, B.H., Frette, K. Stamnes and J. J. Stamnes, *Modeling optical properties of human skin using Mie theory for particles with different size distributions and refractive indices.* OPTICS EXPRESS, 2011. **19**(15): p. 14549-14567.

50. Nobrega, S. and P.J. Coelho, *A parametric study of thermal therapy of skin tissue.* J Therm Biol, 2017. **63**: p. 92-103.

51. Song, J., R.P. Joshi, and K.H. Schoenbach, *Synergistic effects of local temperature enhancements on cellular responses in the context of high-intensity, ultrashort electric pulses.* Med Biol Eng Comput, 2011. **49**(6): p. 713-8.

52. Jaunich, M., et al., *Bio-heat transfer analysis during short pulse laser irradiation of tissues.* International Journal of Heat and Mass Transfer, 2008. **51**(23-24): p. 5511-5521.

53. Bashkatov, A.N., et al., *Optical properties of human skin, subcutaneous and mucous tissues in the wavelength range from 400 to 2000 nm.* Journal of Physics D: Applied Physics, 2005. **38**(15): p. 2543-2555.

54. C.R. Simpson, M.K., *Near-infrared optical properties of ex vivo human skin and subcutaneous tissues measured using the Monte Carlo inversion technique* Phys. Med. Biol., 1998. **43**: p. 2465–78.

55. Inc., C. *Modeling of Material Heating via the Beer-Lambert Law.* 2017; Available from: https://www.comsol.com/model/modeling-of-material-heating-via-the-beer-lambert-law-46701.

56. Muratori, C., et al., *Electrosensitization assists cell ablation by nanosecond pulsed electric field in 3D cultures.* Sci Rep, 2016. **6**: p. 23225.

57. Edelblute, C.M., et al., *Controllable Moderate Heating Enhances the Therapeutic Efficacy of Irreversible Electroporation for Pancreatic Cancer.* Scientific Reports, 2017. **7**(1).

58. Bernadette Marrero, S.S., Richard Heller, *Delivery of Interleukin-15 to B16 Melanoma by Electroporation Leads to Tumor Regression and Long-term Survival.* Technology in Cancer Research and Treatment, 2014. **13**(6).

59. Dunki-Jacobs, E.M., P. Philips, and R.C. Martin, 2nd, *Evaluation of resistance as a measure of successful tumor ablation during irreversible electroporation of the pancreas.* J Am Coll Surg, 2014. **218**(2): p. 179-87.

VITA

JAMES MICHAEL HORNEF

EDUCATION

Old Dominion University

Bachelor of Science, in Electrical Engineering *August 2014 – August 2016*

Old Dominion University

Master of Science in Biomedical Engineering *August 2015 – Present*

PROFESSIONAL EXPERIENCE

Frank Reidy Research Center for Bioelectrics

Graduate Research Assistant *May 2015 – Present*

Created biomedical devices for use in several biological experiments, including electrodes and heating devices for IRE ablation of tumors and gene electrotransfer. Primary research focused on the synergistic effect between PEF and laser heating. Performed independent experiments to characterize the optical effects of laser heating on tissue as well as simulations of laser heating in different conditions. Assisted in several biological experiments, optimizing IRE pulsing conditions and collecting electrical data.

Air Force Research Laboratory

Research Assistant *June 2017 – August 2017*

Characterized the properties of a non-thermal, helium jet plasma using a high power Nd: YAG laser and the Thomson scattering technique. Mastered optical alignment procedures of laser/plasma interactions as well optimizing the interaction timing and data collection using a ICCD camera. Independently collected data and performed several variable dependency tests.

PUBLICATIONS

1) (**Peer Reviewed Publication**) C. M. Edelblute, J. Hornef et al., *Controllable Moderate Heating Enhances the Therapeutic Efficacy of Irreversible Electroporation for Pancreatic Cancer*. Scientific Reports 7, (2017).
2) (**Poster Presentation at the 2nd World Congress on Electroporation**) J. Hornef et al., *Controlled Infrared Heating System to Enhance Pulsed Electric Field Treatments,* Proc. of the 2nd World Congress on Electroporation, September 24th–28th 2017 in Norfolk, Virginia
3) (**NASA Technical Report**) Hornef, J., & Lucas, J. (2017). *Design and Calibration of a Raman Spectrometer for use in a Laser Spectroscopy Instrument Intended to Analyze Martian Surface and Atmospheric Characteristics for NASA*. *Ntrs.nasa.gov*. Retrieved 8 November 2017, from https://ntrs.nasa.gov/search.jsp?R=20160006407